BME

BUDAPEST UNIVERSITY
OF TECHNOLOGY AND ECONOMICS

DIPLOMA THESIS

Investigation of Total Body Irradiation Techniques Using Linear Accelerator

Dominika Eleonóra Kis

Supervisor: Dr. Tamás Pócza
medical physicist
National Institute of Oncology, Hungary

Departmental consultant: Dr. Csilla Pesznyák
associate professor
BME Faculty of Natural Sciences
Institute of Nuclear Techniques

BME

FACULTY OF
NATURAL SCIENCES

2026

MŰEGYETEM 1782

Selection of thesis topic

Student: Dominika Eleonóra Kis	**Specialization:** Orvosi fizika MSc
Organizing department of the final exam: NTI	

Supervisor: dr. Tamás Pócza – Institute: National Institute of Oncology – Title: clinical medical physicist – Email: pocza.tamas@oncol.hu	**Internal supervisor: Dr. Csilla Pesznyák** – Department: NTI – Title: associate professor – Email: pesznyak@reak.bme.hu

Topic: Investigation of Total Body Irradiation Techniques Using Linear Accelerator

Brief description of the topic and list of the main tasks to be solved:

The National Institute of Oncology has 30 years of clinical experience with total body irradiation. However, in recent years, the range of available technical solutions has expanded significantly, which may make it possible to discontinue the use of the currently applied Co-60 isotope and to introduce treatments performed with a linear accelerator into routine clinical practice.

The student's tasks::

1. To perform a literature review on the topic and investigate the clinical applicability of total body irradiation techniques at our institute.
2. To analyze the possibilities of patient positioning and immobilization, and to assess their clinical feasibility.
3. To investigate the applicability of different imaging modalities for the delineation of target volumes and organs at risk.
4. To compare treatment plans created with different irradiation techniques with regard to target volume coverage and organ-at-risk sparing.
5. To plan, perform and analyze quality assurance measurements for the different techniques using dosimetric phantoms.

Final exam topics:

Radiotherapy

Date: 2026. 05. 28.

Signature of Student:	**Signature of Supervisor*:**	**Signature of Internal supervisor:**	**I approve the topic. Signature of the Head of Department:**

*By signing the present thesis topic announcement, the supervisor acknowledges that, pursuant to Sections 145 and 146 of the BME Code of Studies and Examinations, the University considers the public availability of BSc and MSc theses to be the primary principle in order to achieve the educational objectives. Access may be restricted only in exceptional cases, with the prior approval of the Dean.

Declaration of originality

Undersigned Dominika Eleonóra Kis, medical physics MSc student of the Budapest University of Technology and Economics, declare that I wrote this thesis without the use of any unauthorized assistance, under the guidance of my supervisor.

I have cited every source I used. For any part that I have borrowed verbatim, or paraphrased while preserving its original meaning, I have marked its source of origin.

2026.05.21.

Identicality of digital and printed versions

Undersigned Dominika Eleonóra Kis, medical physics MSc student of the Budapest University of Technology and Economics, declare that the digital and printed copies of the thesis are identical in all respects.

2026.05.21.

Contents

1 Introduction

1.1 History of Radiotherapy

Even though Plucker noticed apple-green, glowing traces on the inner wall of a vacuum tube in 1859 [1], it was Wilhem Conrad Röntgen's observation in his laboratory on November 30, 1895 [2] of the luminescence of a fluorescent screen as a result of invisible rays called X-rays that marked the beginning of a new era in medicine. Only three weeks after the publication of Röntgen's discovery, on January 29, 1896, Emil Hermann Grubbe, at the suggestion of Dr. Ludlam, administered what is widely considered the first therapeutic X-ray treatment [2]. In 1896, Leopold Freund treated a patient with a hairy nevus every day for two weeks, after he realized that the X-rays cause epilation; this case is known as the first fractionated radiotherapy in history.

The discovery of the previously unknown phenomenon of radioactivity by Henri Becquerel in 1895 occurred almost simultaneously with Röntgen's discovery of X-rays [1]. In 1898, Pierre and Marie Curie discovered the radioactive element radium, and not soon after, in 1901, Becquerel's skin got inflamed as a result of carrying radium in his pocket. This accident motivated Curie to make experiments on his own skin; their observations led to the birth of radium therapy [1]. Two main types of apparatus emerged for these therapies: plaques covered with radium salts for external application to the skin, and tubes containing radium salts for insertion into tumors or body cavities [1]. Such were the beginnings of brachytherapy.

In the first years of radiotherapy, scientists and doctors lacked the understanding of the biological effects of radioactive materials, let alone the term radiation dosimetry. The first known attempt to measure radiation was carried out by Guido Holzknecht in 1902, with a machine called chromoradiometer [2, 3]. It took over two decades before the first physical unit of exposure, the roentgen, was formally adopted at the first International Radiology Congress in Stockholm in 1928 [2, 3, 4], along with the use of ionization chambers [2, 3].

Claude Regaud's experiments in 1911 demonstrated that fractionated doses could achieve superior biological effects compared to single-occasion treatments [2, 5]. His collaboration with Henri Coutard in the Radium Institute of Paris led to the development of various radium therapies using low dose rates and fractionation [2, 5]. They presented their results at the International Congress of Otology in Paris in 1922, demonstrating cure of advanced laryngeal carcinomas [2]. Coutard's clinical work meant a huge improvement in radiotherapy and established the principles of modern fractionation, including the importance of proper patient immobilization [2]. Ralston Paterson in 1931, as a director of the Holt Radium Institute, started to develop

a treatment standard that would later become known as the Manchester School; he introduced standardized field arrangements and dose tolerance limits [2]. The next decades (1930s-1950s) were marked by the development of mainly brachytherapeutic techniques using radium and X-ray tubes producing 50 kV-200 kV of energy [4].

The next three decades were the so-called megavoltage era [4], where ^{60}Co units were introduced [4, 5], providing superior penetrating power and skin sparing compared to orthovoltage equipment [3, 4]. At the same time, the first clinical linear accelerator, also known as LINAC, began operation at Hammersmith Hospital in 1953 [3]. As linear accelerators became commercially available, doors opened in front of medical researchers to develop various irradiation techniques for the wide spectrum of malignancies.

A Brief History of Total Body Irradiation

R. Abbe (1903) and N. Senn (1903), among others, conducted experiments to treat leukemia, and the latter realized that the irradiation of the whole body was necessary [6]. F. Dessauer (1905) developed a scheme for X-rays to irradiate the whole body, and H. Heineke treated patients with leukemia and sarcoma in the same year using the same principle [6].

Although the developments aforementioned were truly innovative, the modern era of total body irradiation (TBI) began with E. Donnall Thomas in 1957, who systematically combined TBI with bone marrow transplantation [6, 7]. Thomas' study of 100 acute leukemia patients in 1977 established TBI as a truly useful conditioning regimen combined with chemotherapy [6, 8]. In 1979, Thomas reported a 60% 3-years survival rate for patients in first remission [6, 9]. Thomas' work, recognized with the 1990 Nobel Prize [6], transformed TBI from an experimental radiation therapy technique into an important component of modern transplantation medicine.

The technique evolved from simple opposing field arrangements using basic X-ray equipment in the early 1900s to sophisticated intensity-modulated radiation therapy (IMRT) applications introduced by J.T. Keane in 2000 [10], followed by helical tomotherapy and volumetric modulated arc therapy (VMAT) in the following years [6].

1.2 Radiobiological Background of Total Body Irradiation

The biological effects of ionizing radiation primarily result from two mechanisms: direct and indirect actions. In direct action, the energy of the radiation is deposited directly into the critical biological targets, particularly DNA, causing immediate damage in the molecules of these structures [11]. During indirect actions, other

cellular molecules are damaged, which then diffuse far enough and reach potentially critical targets as well. Mammalian cells consist of 70-80% water, hence most of the indirect effects happen through free radicals of water molecules [11]. These free radicals will react with the DNA, leaving them damaged and chemically reactive; in the presence of oxygen, O_2 will react with these molecules [11].

The whole process is illustrated in Figure 1. During direct action, the particles of the radiation ionize the critical targets directly, e.g. the DNA [11]. Most of the indirect damage occurs through the radiolysis of water molecules, when the free radicals after the ionization diffuse to the previously mentioned critical targets and react with them, making them chemically reactive (this part of the target is denoted by $R^\bullet$ on the figure) [11]. In the presence of oxygen, O_2 reacts with this reactive part of the target and produces $RO_2^\bullet$, which participates in another chemical reaction, leading to ROOH [11]. This way, the critical target is not chemically reactive anymore, but its structure changed and it will be recognized biologically; it is a lesion [11].

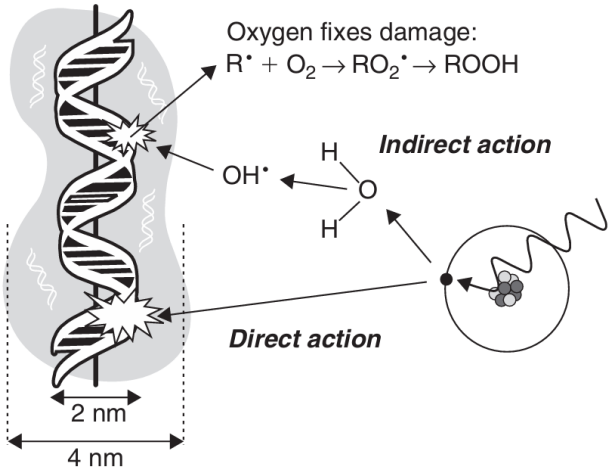

Figure 1: Processes of radiation damage - direct effect and indirect effect in the presence of O_2 [11].

If oxygen is not present, or not in a sufficient concentration, the $R^\bullet$ molecule will eventually react with H^+ [11]:

$$[R-H] + OH^\bullet \rightarrow R^\bullet + H_2O \tag{1}$$

$$R^\bullet + H^+ \rightarrow [R-H] \tag{2}$$

As shown by the equations, the damaged target could be repaired biologically through a purely chemical process [11]. In these cases, there will not be further biological effects. That is the reason why it is harder to damage tissues with hypoxia — these tissues require approximately 2.5-3 times the radiation dose to achieve the same biological effect as well-oxygenated tissues [12].

As a result of radiation exposure, DNA can become damaged, and suffer from either a single strand breakage (SSB) or double strand breakage (DSB) [13, 14, 15]. While SSBs are readily repaired and generally do not result in cell death [15], double strand breaks could potentially lead to chromosomal aberrations, genetic disorders in the progenies, or cell death [16, 17]. The complexity of DNA damage increases

with radiation dose, leading to clustered damage sites that are more difficult to repair accurately [16, 18].

Mammalian cells have evolved two primary mechanisms for DSB repair: non-homologous end joining (NHEJ) and homologous recombination (HR) [19]. NHEJ is active throughout the whole cell cycle and it is the predominant repair pathway, especially during the G1 phase when the HR is not active at all [20]. Unfortunately, NHEJ is intrinsically error-prone, it might introduce small deletions or insertions at the repaired parts [20]. In contrast, HR requires the presence of sister chromatids and is therefore most active during S and G2 phases of the cell cycle [21]. The efficiency of DNA repair differs markedly among cell types and constitutes a major determinant of cellular radiosensitivity [22]. Normal somatic tissues typically maintain effective DNA damage response and repair pathways, whereas many malignant cells, including hematopoietic malignancies treated with TBI, harbor alterations or deficiencies in these mechanisms [23] that contribute to genomic instability and variable radiation sensitivity [24, 25, 26]. Such differences in DNA repair capacity, together with the potential for hematopoietic rescue following stem-cell transplantation, underlie the therapeutic window exploited in TBI conditioning regimens [27].

Radiation-induced cell death can proceed via multiple pathways [28]. In hematopoietic tissues, apoptosis is a major mechanism of radiation-induced damage, although other pathways (such as senescence or stem-cell exhaustion) may also contribute [29]. Apoptosis is a highly regulated process triggered by p53-dependent pathways following DNA damage detection [29]. The p53 protein initiates either DNA repair mechanisms for repairable damage or apoptotic pathways when damage exceeds repair capacity [28]. Programmed cell-death pathways, particularly apoptosis, are especially prominent in lymphoid lineages and contribute to the high radiosensitivity of these tissues [24, 30]. Bcl-2 proteins are very important in regulating apoptosis: pro-apoptotic proteins like Bax promote cell death, whereas anti-apoptotic members such as Bcl-2 provide cellular protection [31]. Variations in apoptotic susceptibility, potentially due to differences in the expression or activity of Bcl-2 family members, may contribute to the observed heterogeneity in treatment responses among patients.

Cell survival following radiation exposure can be described by the linear-quadratic (LQ) model, expressed as $S(D) = \exp(-\alpha D - \beta D^2)$, where $S(D)$ is the surviving fraction at dose D, α describes the linear component of cell killing, and β represents the quadratic component [32]. The α/β ratio characterizes tissue radiosensitivity and repair capacity. Tissues with low α/β ratios exhibit greater capacity for sublethal damage repair and are more sensitive to changes in fractionation, while tissues with high α/β ratios show less fractionation sensitivity [33, 34]. Hematopoietic cells, the primary targets in TBI for conditioning regimens, generally exhibit high

radiosensitivity characterized by high α/β ratios and limited repair capacity [35]. Significant heterogeneity exists among different leukemic cells, with survival fractions after 2 Gy ($S(D)$) ranging from highly sensitive ($S(D) < 0.1$) to relatively resistant ($S(D) > 0.5$) populations [35]. This variability has important implications for treatment outcomes and suggests that individual patient factors may influence TBI efficiency [35].

The major dose-limiting toxicities in TBI predominantly affect late-responding tissues characterized by low α/β ratios and high sensitivity to fraction size [35]. Critical organs include the lungs (pneumonitis), kidneys (nephritis), liver (veno-occlusive disease), and central nervous system [35]. These tissues exhibit marked sensitivity to changes in fractionation parameters, so giving careful attention to dose rate and fraction size is essential for minimizing complications [35]. The radiobiological basis of developmental effects in children receiving TBI remains incompletely understood but likely involves damage to slowly proliferating stem cell populations with finite division potential [35]. These effects cannot be adequately predicted by conventional radiobiological models developed for rapidly dividing cell populations [35].

1.3 Indications of Total Body Irradiation

The use of TBI as a part of conditioning regimens for hematopoietic stem-cell transplantation (HSCT) is grounded in three principal indications: eradication of residual malignant cells even from sanctuary sites (e.g. central nervous system, testicles), immunosuppression to prevent graft rejection, and creation of marrow space for donor engraftment [27]. Several reviews and guideline documents have delineated these indications in the context of treating hematological diseases [36, 37].

First of all, TBI provides a homogeneous radiation dose across the body that can reach so-called sanctuary sites (for example, the central nervous system, testes and other extramedullary sites) where chemotherapy delivery is often limited [27, 38]. In the context of acute lymphoblastic leukemia (ALL) and other high-risk leukemias undergoing myeloablative conditioning before allogeneic HSCT, TBI can reduce the risk of relapse [39].

Beyond its cytotoxic effects, TBI contributes to the immunosuppression of the host, thereby reducing the risk of graft rejection [40]. Because irradiation affects lymphoid tissues ubiquitously, it complements chemotherapeutic agents in achieving a sufficiently immunodepleted environment to allow donor hematopoietic stem cells to engraft [27]. In particular for patients who receive haploidentical or mismatched donor grafts, TBI-based conditioning has been shown to provide better engraftment and survival outcomes [41].

In addition to its immunosuppressive role, TBI helps to create physical and bio-

logical "space" in the recipient's bone marrow micro-environment by ablating host hematopoietic stem/progenitor cells and making room for donor stem cell populations [27]. As such it is routinely employed in myeloablative regimens for both malignant (e.g. ALL, acute myeloid leukemia, lymphomas) [36] and selected non-malignant disorders (e.g. severe aplastic anaemia) [42].

Despite the clear advantages of TBI, its application must be considered in the context of patient-specific risk factors (like age and comorbidities), disease characteristics (like leukemia type or prior therapy) and donor/graft factors. Recent data suggest that in patients who are minimal-residual disease (MRD) negative pre-transplant, non-TBI regimens may yield similar outcomes, whereas MRD positive patients derive distinct benefit from TBI-based conditioning [43, 44].

2 Previous Methods in the Literature

2.1 Methods Using ^{60}Co

^{60}Co teletherapy units were the first devices used for TBI. The choice of this radioactive isotope for the machines was motivated by several advantages. The output of these teletherapy machines is stable and predictable. The ^{60}Co isotope emits γ-rays of approximately 1.17 MeV and 1.33 MeV energy [45], resulting in a mean photon energy of approximately 1.25 MeV; this high energy makes deep penetration and skin sparing possible [46]. The relatively long half-life of ^{60}Co (1925.28 days [45] which is approximately 5.27 years), as well as the achievable high specific activity of it, makes it convenient for the clinical use [47]. Further advantage of the use of a radioactive isotope for teletherapy in general is that the source of radiation is independent of power supply; this can be a key component of cancer treatments in developing countries.

The drawbacks of using ^{60}Co mirror some of its advantages. Due to their decay, they have to be replaced and recalibrated frequently; this may require significant financial and human resources. Their power supply independency can be a possible radiation safety hazard, since it can never be completely shielded, it cannot be turned off totally with the press of a button, and the source must be handled as radioactive waste after disposal. A further problem with machines using ^{60}Co has direct clinical relevance: the modulation capability is limited. The dose distributions are mainly shaped through physical shielding and compensators, so the opportunities for the shielding of organs at risk are limited. Furthermore, since the source is not a perfect point source, a wide penumbra can be formed.

The most common technique involving ^{60}Co uses an extended SSD to cover the entire patient with a single field. In these cases the source is about 2.5 m above the

floor [48], yielding a possible field size of $\sim 1.3 \times 2.7$ m^2 on the treatment plane without interleaved collimators [48]. If the patient is exposed to the field from a lateral direction, boluses are used to ensure that thinner parts, such as the neck, do not receive too high doses [49]. There are methods where the patient is standing in the field instead of lying on couch [50], usually because the treatment room is not high enough, but is long enough for this setup to provide a field wide enough. This kind of treatment could cause more discomfort to patients in poor condition than if they were laid.

To address longitudinal dose variation, some centers utilize the continuous head-swivel motion of a cobalt unit [51]. The cobalt head rotates slowly about its vertical axis while the patient lies supine on a couch, ensuring the entire body receives a composite dose from a sweeping beam. With this method, longitudinal homogeneity within $\pm 10\%$ can be approached without complex compensators [51].

2.2 Methods Using LINACs

LINACs are widely used in radiotherapy, including TBI. High energy electrons and photons can be produced by them, which are suitable for tumor irradiation.

Their operation is based on accelerating electrons in a linear waveguide, hence the name. A LINAC contains several major subsystems working in sequence; the main parts are presented in Figure 2.

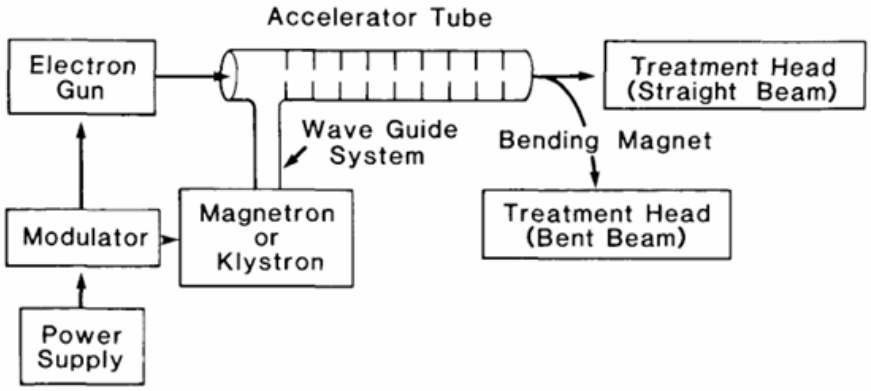

Figure 2: Block diagram of a medical LINAC [52].

The *power supply* provides high DC-voltage for the entire system. The *modulator* converts this DC power into high-voltage pulses for the electron gun and the magnetron or klystron [52]. The *electron gun* contains a heated cathode which emits electrons; these electrons are injected into the accelerating waveguide [52]. A *magnetron* is a vacuum tube with a central cathode and surrounding resonant cavities. When a strong magnetic field is applied, electrons emitted from the cathode spiral around, inducing electromagnetic oscillations in the cavities. This generates microwaves at

a precise frequency (typically ≈3 GHz [52] for medical LINACs) [52]. The *klystron* is a microwave amplifier — it does not generate RF power on its own but takes a low-power RF signal (from a driver oscillator) and amplifies it [52]. It contains multiple cavities which the electrons pass through and they become velocity-modulated (bunched) [52]. This bunching causes energy transfer from the electron beam to the RF field [52]. Either a magnetron or a klystron provides the alternating electric field to the *accelerator tube* where the electrons will gain energy thanks to the alternating electromagnetic field [52]. After the electrons are accelerated, the beam is focused and, if required by the arrangement of the machine, bent using *bending magnets* [52]. This ensures the energy selectivity as well as the correct direction of the beam. Additionally, depending on the desired particle species, either a high-Z target (e.g. tungsten) or a scattering foil is inserted into the beam's path, resulting in the production of photons via bremsstrahlung or a scattered electron beam, respectively [52].

The main advantages of LINACs compared to equipment using ^{60}Co are the higher achievable photon energies, the versatile beam configurations, and the integration with digital planning systems. Thanks to these advantages, a wide variety of techniques using LINACs have been developed for TBI.

The techniques using *extended-SSD and static fields* mirror the techniques using ^{60}Co. In these approaches, the field provided by the LINAC is static and the SSD is usually at least around 300-400 cm [52] to encompass the patient's full length. There are two main methods for this kind of delivery; the AP/PA (anteroposterior/posteroanterior) and the lateral (or bilateral) methods [52]. During the AP/PA delivery, patients are positioned either standing or supine with two opposing fields [52]. Beam-spoilers are used to increase the surface dose and manual compensators (e.g. bolus, lead sheets) over thinner regions (e.g. head, ankles) are used to maintain dose homogeneity [52].

Thanks to the advancements both in planning software and in the treatment delivery systems, *three-dimensional conformal and intensity-modulated techniques* appeared in the field of TBI. These kinds of techniques improved the dose homogeneity and the OAR (organs-at-risk) sparing. One of these types of techniques is Helical TomoTherapy where a ring-gantry continuously rotates the beam around the supine patient while translating the couch. This method generates highly uniform dose distributions and allows precise lung, kidney, and lens sparing [53]. With these machines "volumetric gradient dose matching" (VGMT) can be used, resulting in smooth junctions [54]. From the perspective of this work, the most relevant of intensity-modulated techniques is volumetric modulated arc therapy (VMAT). This technique uses multiple full or partial coplanar arcs and multileaf collimators to modulate dose intensity. Multiple isocenters and overlapping arcs are used in

general, but the range of actual implementations is quite wide, since every institute can implement its own approaches differently depending on the equipment, planning system, local protocols and other resources in general.

3 Previous Method Applied by Our Institute

At our institute, TBI is performed using ^{60}Co to deliver the prescribed 12 Gy, with extended source-to-surface distance. The treatment follows an in-house protocol. The method relies on determining water equivalent thickness (WET) or distance (WED) along the patient's body and applying correction factors to estimate point doses, mean doses and maximum doses.

Water equivalent thickness represents the effective thickness of tissue, accounting for attenuation properties relative to water. In this setup, a detector is positioned below the patient (or phantom) to measure the attenuation of the photon beam. The attenuation is related to the equivalent thickness of water that would produce the same reduction in beam intensity.

Calibration is performed using a phantom composed of two 10 cm thick slabs, which are slightly shifted relative to each other, allowing attenuation to be measured for known thicknesses. A calibration curve is created using an $x - y$ recorder (autograph), such that a displacement of 1 cm corresponds to a 10 cm change in water-equivalent thickness, establishing the relationship between signal and thickness. Using this method, based on the local results, the average adult water equivalent thickness is typically 20–22 cm.

Water equivalent thickness is measured along the midline from the skull to the pelvis, with additional emphasis on the thoracic region due to the heterogeneity caused by the lungs. The anatomical reference points, where measurements are obtained, are the nasal bridge, the chin, the neck, the jugulum, the mammilla, the xiphoid process, the umbilicus and the symphysis. Measurements are also recorded between these points with sufficient spatial resolution. At the chest (due to the lungs), measurement points are also taken laterally. Here, the edges of the body are also recorded to ensure full anatomical coverage and avoid missing peripheral regions. It should be noted that water equivalent thickness can be directly measured on a CT scan as well, and this method is used at our institute as a substitute for the above-mentioned technique.

From the water equivalent thickness, an Excel sheet calculates the TPR (tissue-phantom ratio). In this protocol, TPR values are normalized such that 20 cm WET corresponds to TPR = 1. Average TPR ($\langle \text{TPR} \rangle$) is calculated using the data obtained from the upper body.

The reference longitudinal zero point is defined at the symphysis, all other anatomical points are measured relative to this position. Due to varying distances from the radiation source, a r^{-2} correction is applied to account for inverse square law effects. Furthermore, the ratio of local TPR to the $\langle \text{TPR} \rangle$ is calculated.

The dose rate at midline is calculated using a reference, calibrated value (10.805 cGy/min), for which correction for time is applied. This dose rate corresponds to $\langle \text{TPR} \rangle = 1$, so the dose rate needs a further correction accounting for the $\langle \text{TPR} \rangle$ differing from 1. Since this technique uses lung shielding blocks, the central dose in lung regions is reduced compared to other tissues. Hence, a correction for this factor is also included in the Excel sheet.

The thinnest lung section closest to the beam axis receives the highest dose. Since the lungs are organs at risk, dose constraints are applied for this sensitive region: the maximum dose here should be 8 Gy. Based on the shielding properties of the block (i.e. what percentage of the radiation is transmitted), the fraction of time the lung is blocked is calculated, as well as the total irradiation time.

The blocks aforementioned are created individually, based on the x-ray image of the patient. The lungs are delineated manually, and since these blocks will be placed on a plexiglass sheet above the patient during the treatment, the size of the blocks is scaled accordingly. The blocks are cast from Wood's metal based on these outlines.

The evaluation of the plan was done through point and mean doses. It should be emphasized that, due to the nature of the technique, these values represent estimations rather than exact dose calculations.
The following parameters were calculated:

- Mean, minimum and maximum point doses of the lungs
- Mean, minimum and maximum point doses of the middle region of the upper body (estimating the dose of the spine)
- Point dose of the nasal bridge (estimating the dose of the cranium)
- Mean, minimum and maximum point doses of the sternum
- Point dose of the pelvis (symphysis) (estimating the rectal dose)

If these dose values are in accordance with the institute's guidelines, the treatment will be delivered during the calculated times, with and without the lung shielding.

4 Newly Developed Method

4.1 Patient Cohort

Since this work's aim is to implement a new technique in a clinical setting, the research was not conducted with current patients, but using retrospective CT scans of patients who previously received craniospinal irradiation or TBI[1]. As a result of this, the scans were usually obtained from head to lower pelvis or upper thighs, with the rare exception of a young child, of whom a whole body CT scan was available.

The scans were chosen based on several factors from a list of sixty-nine patients. Those whose hands were cropped from the scan were excluded, just like the ones that did not contain the whole body in the lateral direction. Since the categorization of patients happened based on their length from the top of the head to the most caudal point of the ischium, all the CTs that ended above this defined lowest point were excluded as well. Patients with arms positioned too far from the body were excluded, too.

After the initial selection, thirty-three patients remained. The above-mentioned axial length was measured, as well as the lateral length, which was defined as the distance between the middle of the humerus bones at the half-point of the axial length. The average axial length was 79.52 cm, with a standard deviation of σ_{length} =12.29 cm. Patients with an axial length of 79.52±12.29 cm were considered "medium" sized, while the patients under and above these boundaries were considered extraordinarily "small" and "big", respectively. The final selection of scans was made subjectively, by selecting patients with the least spread arms possible. Patients were chosen from all three categories to ensure reproducibility, regardless of patient size. The chosen patients got categorized into "small" and "big" groups based on the axial lengths' relation to the average length, to make further evaluation easier.

Patient #7's data arrived later, but since he had a whole body CT, he was included in the patient cohort. The length of this patient was measured from head to toe. The relevant data of the chosen patients are presented in Table 1.

4.2 Immobilization

Since the immobilization directly influences the reproducibility of patient positioning, geometric accuracy, and the uniformity of the absorbed dose, it is a non-negligible component of TBI [55]. Unlike conventional radiotherapy, TBI involves very large fields and long beam-on times, making it necessary to position the patient stably and reproducibly to avoid significant deviations in dose.

Since this study does not include currently treated patients, the immobilization techniques are based on the literature and the institution's previous practices, and

[1] In their case, the scan was originally used to determine the WETs, not to create a VMAT plan using a LINAC.

Patient#	Length[cm]	Width[cm]	Group	Sex
1	76.80	34.24	small	female
2	88.5	38.46	big	female
3	97	50.78	big	male
4	72	30.95	small	male
5	66	26.27	small	male
6	81	41.51	big	female
7	100	25.19	small	male

Table 1: Relevant data of the patients. Length in case of Patients #1-6 is defined as the distance from the top of the head to the most caudal point of the ischium, and defined as the length from head to toe in case of Patient #7. Width was defined as the distance between the middle of the humerus bones at the half-point of the axial length.

have not yet been tested in practice.

With the advent of 3D CT-based planning, it became a natural requirement for the treatment geometry to match the planning geometry [55]. Current workflows therefore use vacuum mattresses, full-body molds, thermoplastic head-shoulder masks, or combinations of these to stabilize the patient [56, 57, 58, 59].

Vacuum mattresses provide high stability and are widely adopted because they provide whole-body support and reduce motion across long treatment times [57, 58, 59]. Unfortunately, our institution lacks this immobilization tool.

Several VMAT-TBI planning studies also used thermoplastic masks to stabilize the head and neck during treatment [56, 57, 58, 59]. Thermoplastic masks and head supports are particularly important for techniques that combine multiple isocenters, as head rotation or neck bending can distort target coverage [57, 58].

Immobilization for VMAT-TBI often incorporates indexed baseplates to ensure reproducible longitudinal positioning and minimize inferior–superior drift [55, 56]. Indexing supports the accuracy of isocenter definition for multi-isocenter VMAT approaches [60].

Rotating tabletops, which enable switching between head-first supine and feet-first supine without repositioning, are reported by several centers [55]. Such rotating couch systems reduce setup error because the patient remains immobilized while the table rotates, preserving the original mold geometry [55]. When couch rotation is used, immobilization devices must be compatible with rotational clearance and must maintain body conformity during rotation.

In the case of this study, a rotatable tabletop will be applied in combination with a head–shoulder mask for adult patients. The former one reduces the setup uncertainties, while the latter one, besides the usual immobilization feature, keeps

the head in a slightly backtilted position, which improves the dose homogeneity by moving the chin away from the lower-neck.

Regardless of technique, immobilization must allow the patient to remain comfortable for the entire treatment, as discomfort can lead to motion [55, 61]. Accounting for this, a thin pillow will also be inserted under the patients' heads to provide as much comfort as possible. The patients' arms should be positioned tightly alongside the torso in order to reduce the overall body width and to facilitate a more homogeneous dose distribution through the homogeneous spacial distribution of the body.

Pediatric patients require special immobilization strategies, such as sedation or anesthesia, due to anxiety, small body size, and limited ability to remain still without assistance [62]. In these cases, treatment should be performed under anesthesia to ensure complete immobilization, just like in case of the former technique employed by the institution. A thermoplastic mask should be used for fixation, with a cutout at the top to allow the instruments needed for anesthesia to be inserted. A knee support or a small cylindrical cushion should be placed under the legs to support a stable lower limb position, while the arms were aligned along the torso. Additionally, a head support cushion can be used to maintain a comfortable head position.

Since this work uses retrospective CT scans, these immobilization devices cannot be taken into account at the current planning process. The patients' positions are far from ideal, so the above-mentioned immobilization methods serve as future guidelines based on the literature. This apparent weakness is actually advantageous from a planning perspective, as methods developed for non-ideal geometry are expected to work even better for ideal geometry.

4.3 CT

CT simulation is very important in LINAC-based TBI, as it defines the anatomical dataset on which planning geometry, field arrangements, and dose optimization are based. Accurate CT acquisition is necessary to ensure that target coverage and organ-at-risk (OAR) sparing reflect the true patient anatomy under treatment conditions.

Since TBI treatments involve extended longitudinal coverage, CT scans must encompass information about the entire body. Standard CT scanners are limited in bore length ($\approx 130 - 150$ cm), so whole-body datasets are typically acquired either through two scans (head-first and feet-first) [56, 57, 58, 59, 63, 64], or with the extension of a head-first scan in the inferior direction by replicating the last slice of the acquired head-first scan [65]. To the author's knowledge, no other articles explicitly document the approach of slice replication. At our institution, the maximum length

of CT scans is 200 cm, which implies that in most cases the scans can be obtained in one position. Although it is an advantage in terms of scanning, the treatment cannot be performed in one position, so this advantage cannot be truly exploited if the patient is too tall. The retrospective scans of this work do not contain adults or teenagers with full-body CT scans, and since the replication of the last slice does not lead to anatomically realistic planning setups, this practice was only followed in case of Patient #4, as an experiment for the planning procedure.

Immobilization devices used during CT simulation must match those used during treatment to maintain geometric consistency. Vacuum mattresses, thermoplastic masks, and indexed baseplates are therefore secured during the scan, and the patient is positioned identically to the planned treatment setup [66]. CT scanning in pediatric cases requires extra attention, since children may require sedation or specialized immobilization to maintain stillness throughout the extended acquisition [67]. Care must be taken to ensure that any immobilization or sedation approach used during simulation can be replicated during treatment delivery.

Most VMAT-TBI planning studies acquire CT images with slice thicknesses of 5 or 10 mm, which provides sufficient spatial resolution for whole-body contouring and OAR segmentation while keeping dataset size computationally feasible. Pierce *et al.*, Symons *et al.*, and Springer *et al.* used a 5 mm slice thickness for planning [57, 58, 65]. Springer *et al.* also used 10 mm slice thickness for three patients [58]. Teruel *et al.* adopted 10 mm slice spacing for automatic VMAT-TBI planning in Eclipse [56]. A recent study from 2024 recommends 5 mm of slice thickness for adults and 3 mm in case of small children [68].

During the initial attempts of planning, multiple CT slice thicknesses, e.g. 0.5 cm, were tested to reach balance between resolution and optimization time. As a result, it was found that a thickness of 1 cm gives the same dose distribution as finer resolutions, apart from statistical uncertainties. Figure 3a and 3b show a visual comparison between dose distributions achieved with different CT resolutions in case of Patient #7. In Figure 4, the difference between the DVHs can be observed.

This result is slightly different from the literature, but it has to be emphasized that 1 cm slice thickness appears in papers, so the conclusion presented here is not blatant. For the sake of feasible running times during optimization, slice thickness was chosen to be 1 cm in case of every patient. It reduced the time required for optimization and dose calculation from 45 minutes to 20 minutes in case of Patient #7. These runtimes are specific to the local treatment planning system configuration described in the planning section and should therefore not be interpreted as generally applicable values.

(a) 1 cm (b) 0.5 cm

Figure 3: Achieved dose distribution with 1 and 0.5 cm of CT slice thickness (Patient #7).

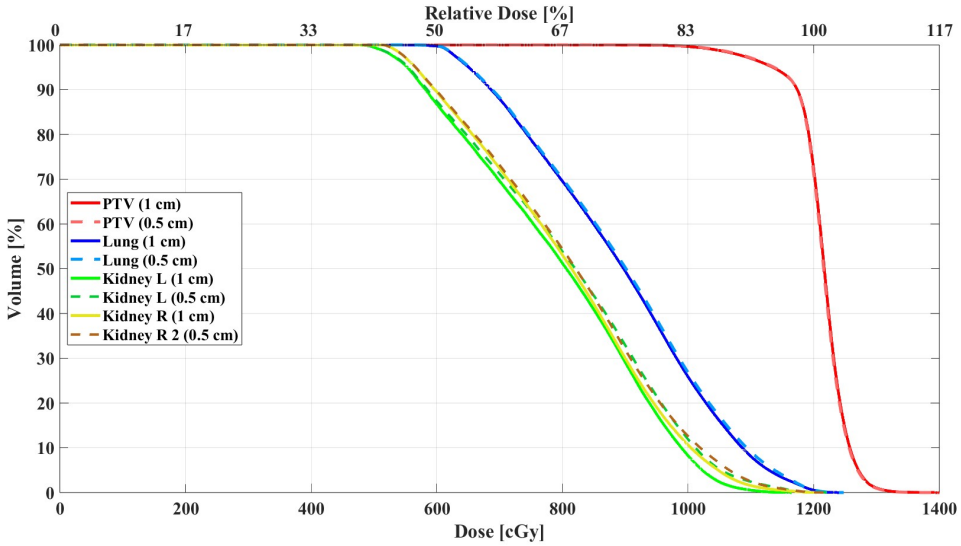

Figure 4: Achieved DVH with 1 and 0.5 cm of CT slice thickness (Patient #7).

4.4 Target Volume and Organs-At-Risk Determination

For TBI, the target is not a tumor-specific volume but the entire external patient contour, modified only where organ sparing or dose limitations are clinically justified.

The rationale is that in TBI the goal is the irradiation of the whole body for conditioning, so the PTV must represent that large volume. Many modern TBI planning studies shrink the body external contour by 3-5 mm when defining the PTV [56, 57, 65, 69]. The primary reason behind it is that the superficial region has more dosimetric uncertainty due to the build-up effects and the air gap, so

contracting gives a safety margin through providing backscatter media. In this work, the body contour has been contracted by 5 mm in case of adult and teenage patients, and by 4 mm in case of young children.

Even though the target is essentially the whole body, there are some organs that usually are excluded from the PTV. Most commonly these are the lungs and the kidneys. Lungs, since radiation induced pneumonitis can be a very burdensome complication for the patients with suppressed immune systems, and kidneys, since renal dysfunction may appear later in life, worsening their quality of life. For optimization purposes, the contour of the OARs is shrunk by a few millimeters (2-3 mm in case of kidneys and 3-5 mm in case of lungs [56, 57]), so the planning system has a few millimeters of space to reduce the dose at relevant places. In this work, the size of the margins was 2 mm for kidneys, and 5 and 4 mm for lungs in case of adult/teenagers and little children (Patient #7 here), respectively. In the case of Patient #7, the size of the margins was reduced to ensure that the ratio of the omitted volume to the total body volume was close to that of adults. As an example, the relevant contours of Patient #7 are shown in Figure 5.

It is important to denote that the purpose of the cropped contours is to make the planning and optimization process more stable, and not to articulate the biological importance of certain regions of an organ. Consequently, the dosimetric results should always be interpreted for the entire organ, not for the shrunken contour.

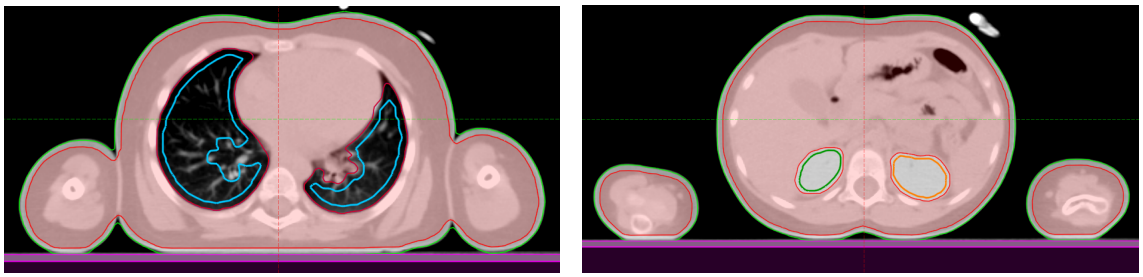

(a) Contour of the lungs (blue)

(b) Contour of the kidneys (dark green and orange)

Figure 5: Contours of Patient #7. The body contour is green, the PTV contour is red.

4.5 Planning

In LINAC-based TBI, planning aims are to generate a homogeneous dose distribution over the entire patient while respecting dose constraints for radiosensitive organs [66]. Since TBI involves large treatment fields, complex patient geometry, and multiple treatment isocenters, the planning process should be standardized [68] and reproducible with well-defined immobilization and simulation steps [55] to make it safe and clinically feasible, especially regarding the required planning time [70].

VMAT-TBI workflows rely on multi-isocenter arc arrangements to compensate for the limited field size and to achieve longitudinal dose uniformity [58, 68]. The

treatment geometry is predetermined by the CT acquisition, after which the body is segmented into overlapping regions, each associated with one isocenter or isocenter group [56, 57, 58]. To provide lateral dose coverage and homogeneity, sometimes more than one isocenter is used in this dimension (hence the term isocenter group) [58]. Junction robustness between adjacent isocenters can be critically important, since any misalignment may lead to local over- or underdosage [58, 70, 71]. For this reason, planning studies typically use generous overlaps between arc fields [71]. Moreover, during dual-arc setups, two arcs are used with the given isocenter, usually with opposite direction of rotation. On average, these approaches provide better dosimetric results [72].

The planning process of this work required significant attention, since field arrangement protocols vary from institute to institute, and the only way to adapt it to the opportunities of our institute was through trial and error. Prior to conducting our own trials, many of the field arrangements mentioned in the literature were tested, but they led to "errors" rather than sufficiently homogeneous dose distributions. A complicating factor in such trials is the diversity of treatment planning systems, as differences in dose calculation algorithms and optimization methods limit the direct transferability of planning protocols between institutions. In this work, the planning protocol was developed using Varian Eclipse treatment planning system.

As a result of our own trials, the process should be discussed separately for patients below and above 115 cm in height. The process was developed for patients above this height, since these kinds of data were accessible. Later, as Patient #7's data became available, the planning procedure could be simplified for cases where the body height is lower than 115 cm.

The planning required multiple isocenters, spaced $\Delta z \approx 17.71$ cm apart (range: [13;33] cm) in the z-direction, covering the patients from the neck to the lower pelvis in case of patients above 115 cm body height. The reason behind the fairly close isocenters is to give enough degrees of freedom to the optimization software to cover a body in its full width and depth. In the x-direction, isocenters were placed on the patient's midline. Due to the geometry of the machines, the isocenter can be a maximum of 32 cm from the edge of the table. Since the width of the table is 53 cm, the isocenter's maximum distance from the table in y-direction can be maximum 17.93 cm. As a result, in case of a maximum 35.87 cm width, the isocenters can be placed in the center of the patient in the anteroposterior direction. Even obese patients in the database used met this criterion.

Six full arcs were placed per isocenter, half of them with 10° collimation and 6FFF energy, half with 350° collimation and 10X energy. The rationale of the usage of different energies was to provide sufficient dose for both superficial and deeper tissues. The three identically collimated fields were opened in the x-direction in

the following x-ranges: $[-20\text{ cm}; -2\text{ cm}]$, $[-10\text{ cm}; +10\text{ cm}]$; $[+2\text{ cm}; +20\text{ cm}]$, thus ensuring adequate coverage and allowing the optimization software to adequately spare the organs at risk. As an illustration of this field arrangement, see Figure 6.

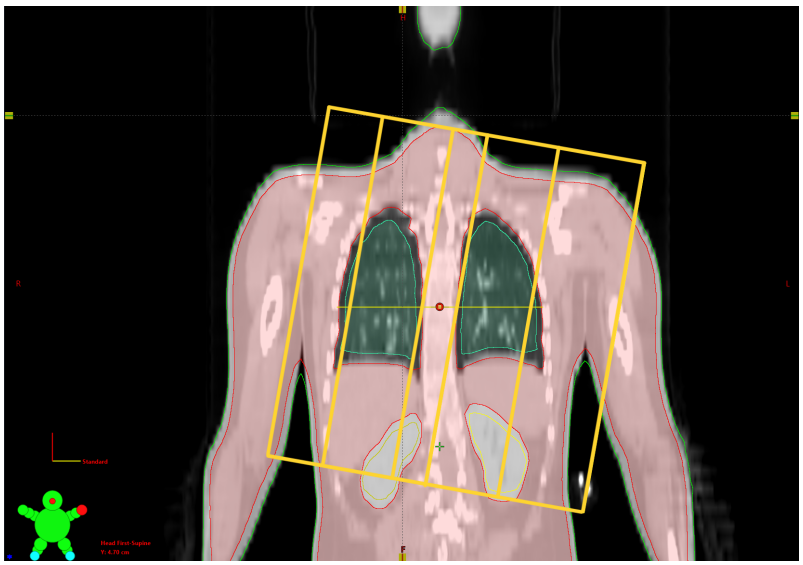

Figure 6: Arrangement of fields with 10° collimation at a given isocenter (Patient #2).

The fields were fully open in the y-direction, and the fields of adjacent isocenters overlapped. Figure 7a, Figure 7b and Figure 7c illustrate the geometry of the field arrangement in axial direction on a patient's left side, middle and right side.

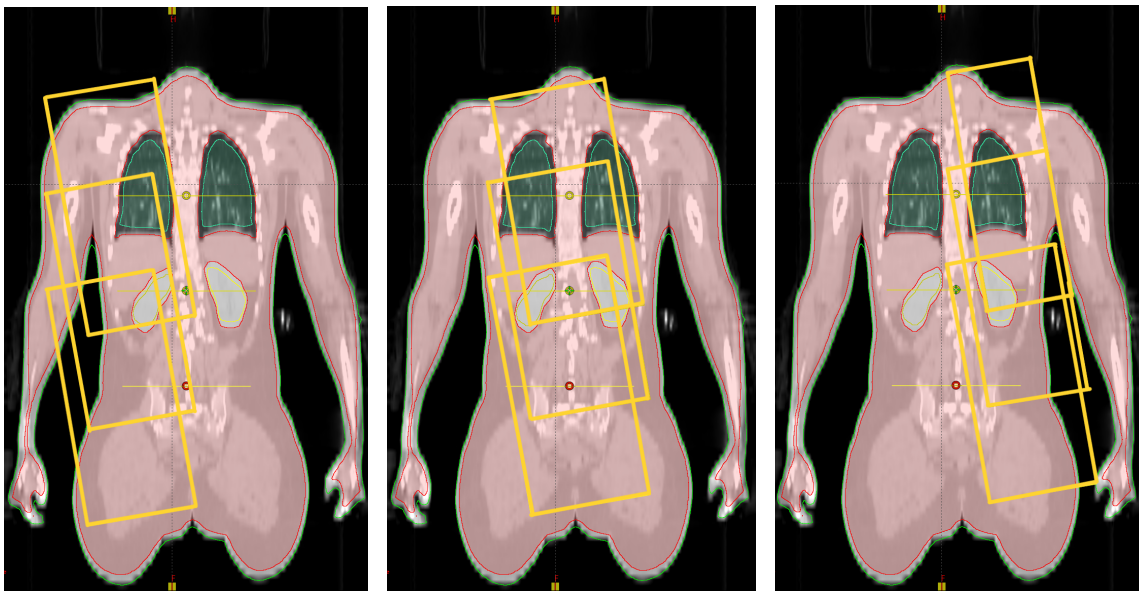

(a) Left side (b) Middle (c) Right side

Figure 7: Field arrangement's geometry in axial direction (Patient #2), showing the fields with collimation of 350°.

In case of patients whose height exceeded 115 cm, the craniocervical region was treated using lateral opposing fields, with gantry rotations of 92° and 268°. The upper legs were treated using AP/PA opposing fields. An obese patient was an

exception (Patient #3), since the hip area was too wide to be covered with AP/PA fields. In his case, VMAT arcs were used at this region as well. The overlaps of the opposing fields with the VMAT fields are illustrated in Figure 8.

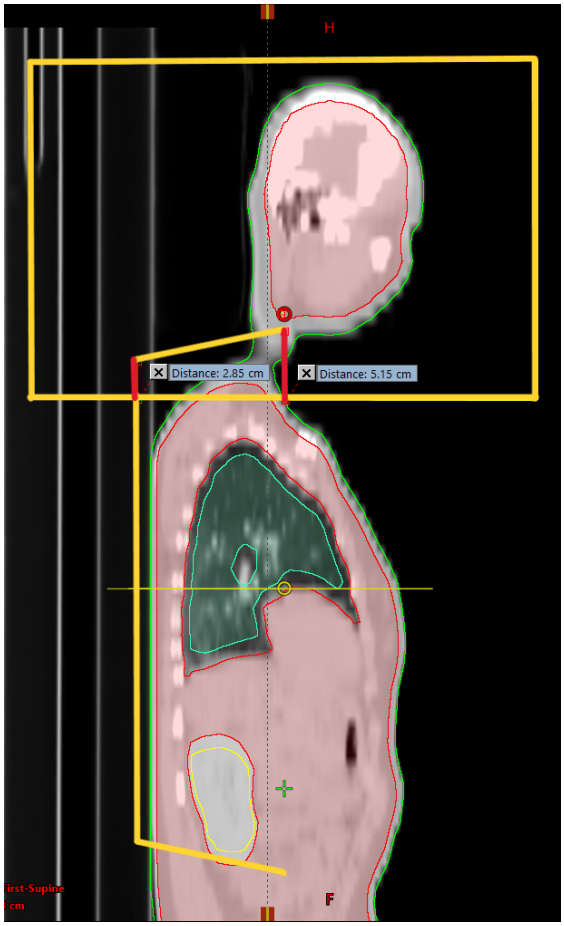

(a) Overlap between the uppermostmost right VMAT field with collimation of 10° and the right field of the craniocervical region.

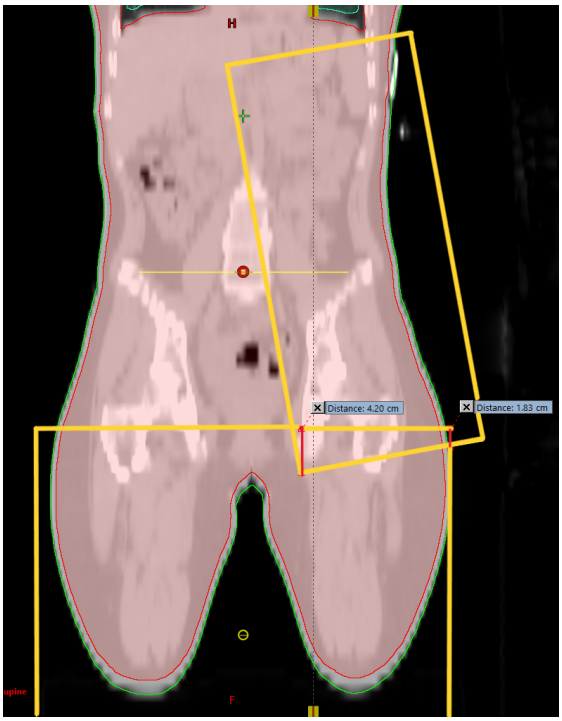

(b) Overlap between the lowermost right VMAT field with collimation of 10° and the right field of the leg region.

Figure 8: Overlaps of static fields of the craniocervical and leg regions with the VMAT fields (Patient #2).

It turned out that in case of small children who did not exceed the total body length of 115 cm, $\Delta z = 33$ cm was sufficient, since fewer degrees of freedom were enough to cover the body in its full width and length. Within the framework of this construction, the machine can treat 3 isocenters using a single patient setup, which is enough to treat the whole body. As a conclusion, in case of patients this small (Patient #7 in this study), VMAT arcs were placed along the entire body. As an example of this field arrangement, see Figure 9.

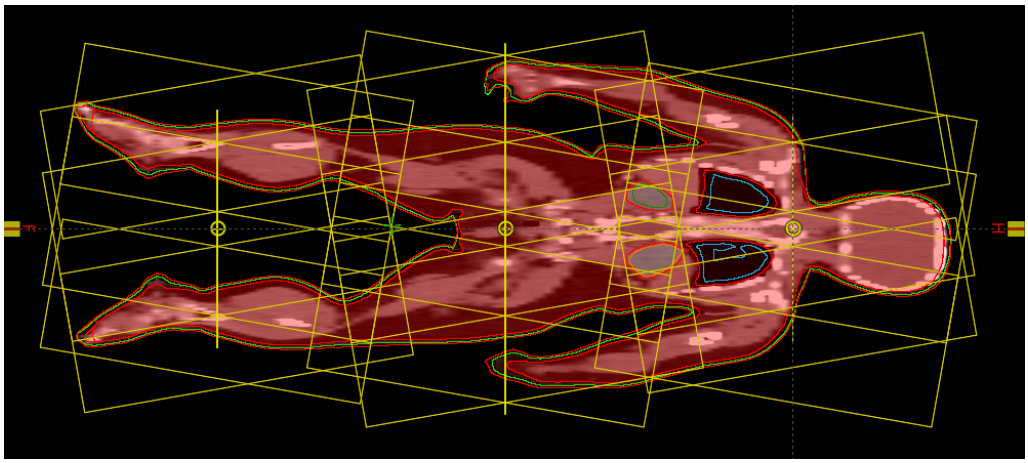

Figure 9: Field arrangement in case of a small patient (height < 115 cm) (Patient #7).

Given the highly modulated nature of VMAT-TBI plans, dose calculation accuracy also deserves especial attention. VMAT-TBI planning commonly uses relatively fine dose-calculation grids (3–5 mm, 5 mm is generally accepted [68]) [57, 70, 73, 74]. According to a general recommendation article (Seravalli *et al.* [68]), the Acuros optimization algorithm is recommended over the AAA algorithm. Despite this, AAA was used in this work, since given the limited computing capacity, it provided more favorable runtimes than Acuros, with a calculation grid of 5 mm. The treatment planning system used the `HybridServiceControl` service connector, which allows calculation tasks to be distributed between local and remote workstations. The control point field parallelization factor was set to 30; this parameter describes how many control-point-related calculation tasks may be processed in parallel. The processor utilization limit was set to 150%, while the physical memory utilization limit was set to 100%, defining the maximum allowed use of the available memory. These settings influence calculation time. The aperture shape control was set to "low" to set a lower bound for the areas marked by the MLCs, hence ensuring a more robust plan delivery. The optimization objectives used for all plans in this work are shown in Table 2.

Structure	Type	Value	Priority
Cropped lung	Mean	720 cGy	90
Cropped right kidney	Mean	720 cGy	90
Cropped left kidney	Mean	720 cGy	90
PTV	Upper limit for D_0	1224 cGy	99
PTV	Lower limit for D_{100}	1200 cGy	100

Table 2: Optimization objectives

The result of investigating the autofeathering feature is quite counterintuitive, as its function would be to smooth the junctions, but the dose distribution seems to be more homogeneous and smooth when this feature is turned off (see Figure 10).

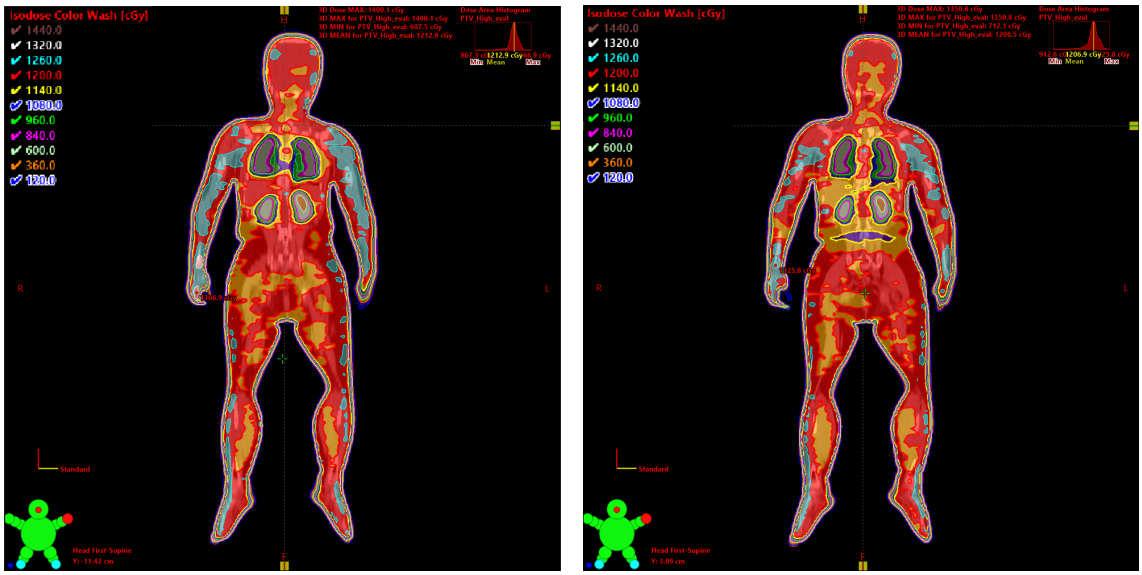

(a) Autofeathering is turned off. (b) Autofeathering is set to 40 cm.

Figure 10: Dose distributions depending on the autofeathering feature.

The smoothing would ideally be achieved through dose profiles with shallower slopes, but the comparison did not show significant difference between the slopes, as the example shows in Figure 11. The difference shown by the profiles is a result of statistical uncertainty, while the expected difference in slopes is absent.

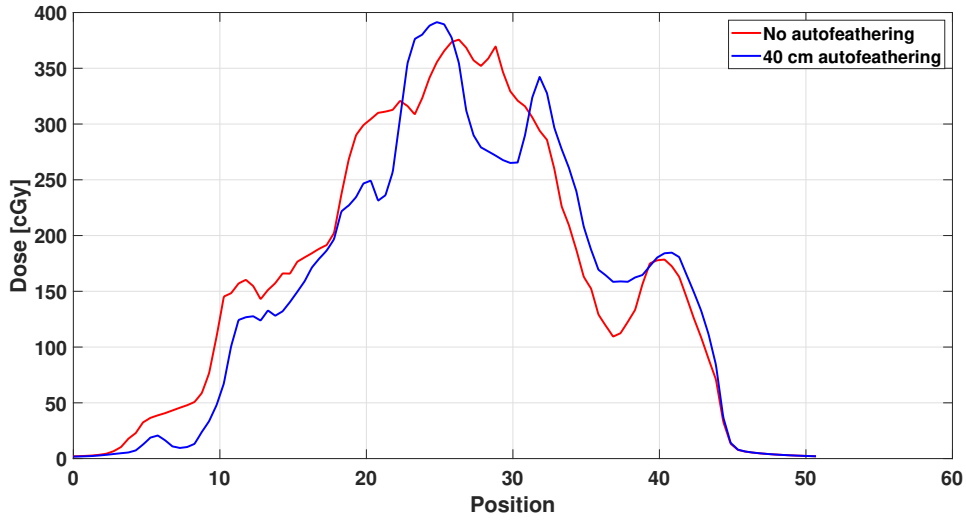

Figure 11: Example of dose profiles of corresponding fields in case of no autofeathering and autofeathering set to 40 cm.

A possible explanation of this phenomenon could be that the autofeathering feature itself was constructed to treat solid tumors, instead of a whole body, which has a significantly bigger volume. However, no mention of this phenomenon could be found in the literature. Probably not every feature of the planning software is optimized for the planning procedures of TBI.

The coverage and maximum-dose metrics evaluated are shown in Table 3.

Patient #	$V_{90}[\%]$	$V_{95}[\%]$	$D_{98}[\%]$	$D_{95}[\%]$	$D_{50}[\%]$	$D_5[\%]$	$D_2[\%]$
1	97.2	92.2	88.49	92.73	102.89	107.12	108.54
4	96.8	90.0	88.19	91.91	102.19	108.38	110.03
5	99.2	96.4	93.08	96.19	102.58	106.65	108.03
Average (small)	97.73	92.87	89.92	93.61	102.55	107.38	108.87
2	88.5	67.3	75.74	83.60	97.26	106.86	110.13
3	81.1	62.6	69.19	75.56	96.82	105.03	107.00
6	96.9	92.1	87.68	92.68	101.53	108.15	109.94
Average (big)	88.83	74.00	77.54	83.95	98.54	106.68	109.02
7 (only VMAT)	97.8	94.6	89.60	94.50	101.40	105.90	107.30
In-house criteria	95<	90<					<110
Literature values	$[98.45, 100.04]$	$[97.42, 99.84]$	$[88.5, 97.5]$	$[89.92, 105.5]$	$[104.16, 106.5]$	115.3	$[108.25, 117.6]$
References	[57, 58, 75]	[57, 58, 75]	[56, 65, 66, 76]	[58, 75, 76, 77]	[66]	[76]	[65, 66, 75]

Table 3: Plan coverage data. Small and big patients are grouped together, and Patient #7 is listed separately, given that the planning method used in their case is different from that of the other patients. Literature value ranges are given as $[\min_i(x_i - \sigma_i), \max_i(x_i + \sigma_i)]$, where x_i denotes the quantity in question for the i^{th} article, and σ_i denotes its standard deviation.

Patient #	$\mathrm{HI}_1 = \frac{D_5 - D_{95}}{D_p}$	$\mathrm{HI}_2 = \frac{D_2 - D_{98}}{D_{50}}$	$\mathrm{HI}_3 = \frac{D_5}{D_{95}}$
1	0.14	0.20	1.16
4	0.16	0.22	1.18
5	0.11	0.15	1.11
Average (small)	0.14	0.19	1.15
2	0.24	0.35	1.28
3	0.30	0.39	1.39
6	0.17	0.23	1.18
Average (big)	0.24	0.32	1.28
7 (only VMAT)	0.11	0.18	1.12
Literature values	0.15	$[0.08, 0.22]$	$[1.14, 1.18]$
References	[76]	[66, 75]	[59, 76]

Table 4: Homogeneity indices. Small and big patients are grouped together, and Patient #7 is listed separately, given that the planning method used in their case is different from that of the other patients. Literature value ranges are given as $[\min_i(x_i - \sigma_i), \max_i(x_i + \sigma_i)]$, where x_i denotes the quantity in question for the i^{th} article, and σ_i denotes its standard deviation.

Plan quality is assessed through indices that capture dose homogeneity as well. The most widely used metric is the homogeneity index (HI), which reflects how evenly the dose is distributed inside the PTV. There are several definitions of the HI, some of which are listed below in Table 4, with the achieved values and literature values. HI_1 was proposed by Kataria *et al.*(2023) [78], but this article discusses the homogeneity index in general, so the presented values there are not relevant in the context of TBI. As a reference value, HI_1 is calculated from data of a relevant article by Venugopal *et al.* (2025) [76]. HI_2 definition is the recommended definition by the ICRU 83 Report, but this report is a general guidance for radiotherapy, not for TBI specifically [79]. The classical definition that is not listed in Table 4 is $\mathrm{HI} = \frac{D_{\max}}{D_{\mathrm{p}}}$, but since it uses the point maximum dose, it is a numerically unstable metric [78]. In spite of this, there are examples of its use in the literature [80]. Near the coverage and the homogeneity of the dose, the doses of the OARs should be taken into account during planning. The achieved doses are shown in Table 5.

Patient#	$\langle D_{\text{lungs}} \rangle$ [%]	$\langle D_{\text{left kidney}} \rangle$ [%]	$\langle D_{\text{right kidney}} \rangle$ [%]
1	71.25	70.25	72.17
4	67.42	66.5	64.92
5	75.50	74.83	75.50
Average (small)	71.42	70.50	70.83
2	67.50	64.75	65.92
3	66.67	63.92	64.42
6	71.00	72.17	72.17
Average (big)	68.42	66.92	67.50
7 (only VMAT)	74.25	66.25	67.25
Literature values	$[60.46, 91.99]$	$[51.29, 90.5]$	$[53.23, 90.25]$
References	[56, 57, 58, 59, 66, 75]	[56, 57, 59, 66]	[56, 57, 59, 66]

Table 5: Doses of organs at risk. Small and big patients are grouped together, and Patient #7 is listed separately, as the planning method used in their case is different from that of the other patients. Literature value ranges are given as $[\min_i(x_i - \sigma_i), \max_i(x_i + \sigma_i)]$, where x_i denotes the quantity in question for the i^{th} article, and σ_i denotes its standard deviation.

4.6 Quality Assurance

4.6.1 Patient Specific Quality Assurance

Patient-specific quality assurance (QA) in VMAT-TBI verifies the agreement between the calculated and delivered dose distributions. In this work, verification was carried out using the DoseCHECK module of the SunCHECK 3.2 (Sun Nuclear Corporation, Melbourne, Florida, USA) software, which provides an independent dose calculation based on the treatment plan parameters. This approach differs from measurement-based QA systems commonly used in the literature (such as ArcCHECK or Delta4 [56, 57, 73, 81]), as it relies on a secondary calculation algorithm instead of detector-based measurements. Since VMAT-TBI plans involve large treatment volumes and multiple isocenters, the use of an independent dose calculation method provides an efficient and clinically practical solution for patient-specific QA without the need for extensive measurement setups.

For each of the seven patients included in this study, gamma index analysis was performed using the DoseCHECK-calculated dose distribution compared to the treatment planning system dose for the VMAT arcs. The gamma index combines dose difference and spatial agreement into a single metric, allowing for a quantitative comparison of two dose distributions. A point is considered passing if both the local dose difference and the distance-to-agreement criteria are satisfied simultaneously [82]. The evaluation was carried out using the commonly accepted gamma criterion of 3%/3 mm, as widely reported in the literature [57, 81], where passing

rates above 95% are generally considered clinically acceptable. Some centers report a stricter criterion (2%/2 mm) [56]. The passing rates are presented in Table 6. In addition to overall gamma passing rates, structure-specific evaluations were performed for the PTV and the OARs, to assess dose agreement in clinically relevant regions.

Patient #	PTV[%]	Lungs[%]	L. kidney[%]	R. kidney[%]	Overall[%]
1	97.55	95.78	100	100	97.41
4	94.32	95.28	100	100	95.94
5	98.35	94.03	100	100	98.35
Average(small)	96.74	95.03	100	100	97.23
2	93.65	94.79	100	100	93.8
3	31.64	71.03	57.4	50.77	33.15
6	44.71	82.6	95.27	90.32	84.26
Average(big)	56.67	82.81	84.22	80.36	70.40
7 (only VMAT)	82.06	98.82	100	100	99.04

Table 6: 3%/3mm gamma passing rates

It has been shown that gamma passing rates do not necessarily correlate with clinically relevant dose differences [83, 84]. Gamma analysis does not capture potential hot or cold spots either, since it allows localized dose discrepancies to be masked, and it does not explicitly indicate the magnitude or clinical relevance of dose deviations within specific regions of interest. Therefore, point and mean dose comparison, as additional evaluation metrics, were also considered, as recommended in the literature [83, 84]. The relative differences between the expected and the calculated point and mean doses are shown in Table 7 and in Table 8, respectively.

Patient#	$\langle \Delta D_{\text{isoc}} \rangle$ [%]	$\Delta D_{\text{max}}^{\text{PTV}}$[%]	$\Delta D_{\text{max}}^{\text{lungs}}$[%]	$\Delta D_{\text{max}}^{\text{l.kidney}}$[%]	$\Delta D_{\text{max}}^{\text{r.kidney}}$[%]
1	-0.10	1.36	2.48	0.24	0.16
4	1.03	2.32	3.66	1.09	0.48
5	-0.20	1.74	3.66	1.20	1.03
Average(small)	0.24	1.81	3.27	0.84	0.56
2	0.53	2.18	2.66	1.03	0.99
3	4.80	3.55	4.40	3.75	4.39
6	2.88	4.96	5.90	4.17	3.19
Average (big)	2.74	3.56	4.32	2.98	2.86
7 (only VMAT)	0.17	2.4	3.63	1.71	1.94

Table 7: Relative differences between the predicted and the calculated point doses. The mean isocenter relative dose difference was calculated by averaging over all evaluated isocenters: $\langle \Delta D_{\text{isoc}} \rangle_i = \frac{\sum_{j=1}^{I} \Delta D_j}{I}$, where I is the number of isocenters, ΔD_j is the relative difference at the j^{th} isocenter.

Patient#	$\Delta \langle D \rangle_{\text{PTV}}$ [%]	$\Delta \langle D \rangle_{\text{lung}}$ [%]	$\Delta \langle D \rangle_{\text{left kidney}}$ [%]	$\Delta \langle D \rangle_{\text{right kidney}}$ [%]
1	1.34	2.42	1.39	1.12
4	2.64	2.97	2.24	2.04
5	1.33	2.82	1.30	1.40
Average(small)	1.77	2.74	1.64	1.52
2	3.08	2.80	2.74	2.57
3	4.96	5.46	7.56	7.13
6	4.08	4.43	4.90	4.91
Average(big)	4.04	4.23	5.07	4.87
7 (only VMAT)	6.70	1.96	1.57	1.31

Table 8: Relative differences between the predicted and the calculated mean doses.

4.6.2 Absolute Dose Test

In this work, absolute dose verification was performed using an anthropomorphic CIRS Thorax Phantom (CIRS Inc., Norfolk, Virginia, USA), similarly to other, published works (e.g. Teruel *et al.* [56]).

The plan of Patient #7 was copied onto the phantom. Since this patient is very small and a one-to-one anatomical correspondence with the phantom could not be achieved, three different configurations were created in order to investigate dose delivery to relevant parts: kidneys, lungs, and the abdomen as a homogeneous part of the PTV. Reference points were defined for every insert, and were named according to the nomenclature used by the IAEA [85].

The measurements were performed using a PTW Semiflex ionization chamber, type 31013 (PTW Freiburg, Freiburg, Germany). This is a cylindrical ionization chamber with a nominal sensitive volume of $0.3\,\text{cm}^3$, intended for reference dosimetry and dose-distribution measurements in radiotherapy water phantoms [86]. Its larger volume gives a relatively high signal, which is useful for stable point-dose measurements, although with reduced spatial resolution compared with smaller chambers. The chamber reference point is located on the chamber axis, 9.5 mm from the chamber tip [86]. PTW specifies a nominal response of approximately 10 nC/Gy [86].

The chamber was positioned with its reference point aligned to the measurement point in the CIRS phantom. After applying the chamber voltage, the collected charge was recorded with an electrometer for each arc investigated. Since the chamber is vented, the reading was corrected for temperature and pressure. In the present measurements, using $p_0 = 101.325\,\text{kPa}$, $T_0 = 20°\text{C} = 293.2\,\text{K}$, $p = 99.65\,\text{kPa}$ and $T = 23.8°\text{C} = 297\,\text{K}$, the correction factor was $k_{Tp} = \frac{Tp_0}{T_0 p} = 1.0299871$. The corrected reading was then multiplied by the calibration coefficient $N_{D,w} = 9.417\,\frac{\text{cGy}}{\text{nC}}$ and the relevant correction factors. For the 10 MV beam, the quality index was 0.742, with $k_Q = 0.977$, $k_{pol} = 1.000$ and $k_{rec} = 1.004$. For the 6 MV FFF beam,

the quality index was 0.629, with $k_Q = 0.996$, $k_{pol} = 1.000$, and $k_{rec} = 1.007$. The absorbed dose can be calculated using these correction factors:

$$D_{w,Q} = M \cdot k_{Tp} \cdot k_{pol} \cdot k_{rec} \cdot N_{D,w} \cdot k_Q \tag{3}$$

, where M is the measured charge in nC.

The measurement arrangement with the Varian Truebeam LINAC is illustrated in Figure 12.

Figure 12: Photos of the measurement arrangement

In the first configuration, the kidney region of the plan was positioned in the central part of the phantom, as shown in Figure 13.

Data was collected using the third and fourth inserts. Since the dose to these points was delivered by the fields of the uppermost and the middle isocenters, these fields were investigated one by one. The fields were named in a way that the first number denotes the isocenter (1: uppermost, 2: middle), the second denotes the

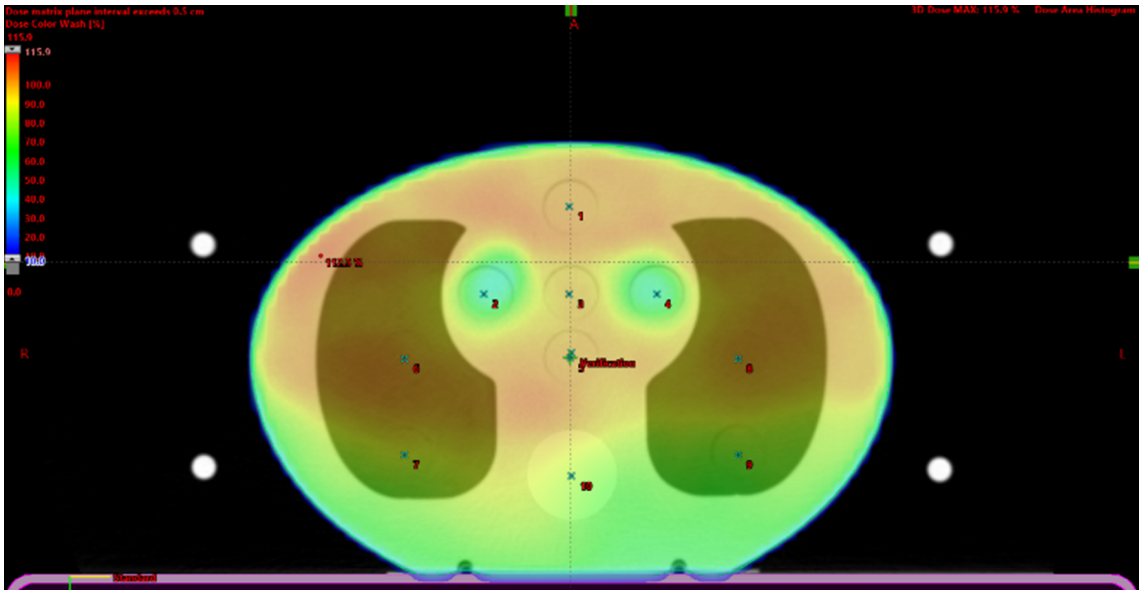

Figure 13: First configuration for the absolute dose test: the kidneys' dose distribution is positioned to the central part of the CIRS phantom to investigate the delivered dose to the kidneys and to the volume between them (inserts 3 and 4)

energy and the degree of collimation (1: 6FFF and 10°, 2: 10X and 350°) and the last one denotes the position of the jaws in the x-direction (1: $[-20\,\text{cm}; -2\,\text{cm}]$, 2: $[-10\,\text{cm}; +10\,\text{cm}]$, 3: $[+2\,\text{cm}; +20\,\text{cm}]$). The calculated and the measured doses with their relative absolute differences from each field at each measurement point in case of the first configuration are shown in Table 9.

Field	Reference point 3			Reference point 4		
	Planned [cGy]	Measured [cGy]	Difference [%]	Planned [cGy]	Measured [cGy]	Difference [%]
1/1/1	6.8	7.51	0.24	8.1	8.08	0.01
1/1/2	82.3	84.9	0.87	25.8	26.14	0.11
1/1/3	0.8	1.75	0.32	0.8	1.66	0.29
1/2/1	0.8	1.35	0.18	1.4	2.02	0.21
1/2/2	58.1	59.94	0.61	13.2	12.22	0.33
1/2/3	6.5	6.81	0.10	14.6	14.74	0.05
2/1/1	1.0	1.81	0.27	1.4	2.16	0.25
2/1/2	51.3	51.16	0.05	14.3	14.52	0.07
2/1/3	24.2	24.32	0.04	27.4	27.40	0.00
2/2/1	8.6	8.56	0.01	14.7	14.19	0.17
2/2/2	55.3	52.62	0.89	23.3	22.90	0.13
2/2/3	0.5	1.01	0.17	0.5	1.04	0.18
Sum	296.2	301.74	1.85	145.50	147.07	0.52

Table 9: Calculated and measured doses inside the left kidney (reference point 4) and between the two kidneys (reference point 3). The relative absolute difference between the planned and the measured doses was normed with the fraction dose (300 cGy).

In the second configuration, one of the lung structures was aligned with a lung-tissue equivalent part of the phantom, as shown in Figure 14.

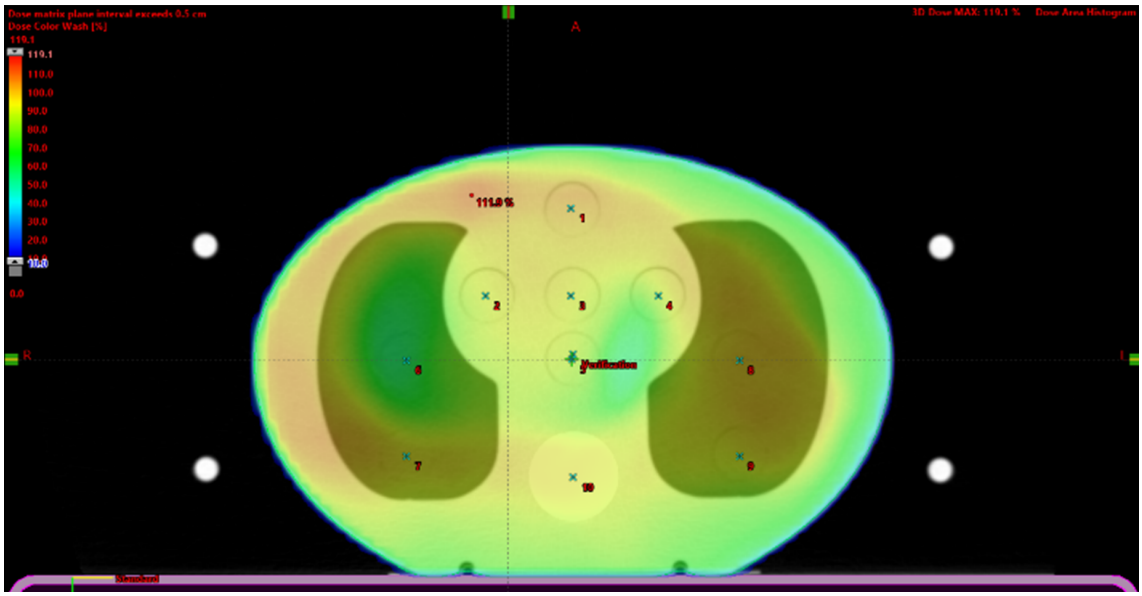

Figure 14: Second configuration for the absolute dose test: the right lung's dose distribution is positioned to the right, lung-tissue equivalent part of the CIRS phantom (insert 6)

In this case, the fourth and sixth inserts were used to place the detector. The dose to these points was also delivered by the fields of the uppermost and the middle isocenters, so these fields were investigated, similarly to the case of the kidneys. The calculated and the measured doses with their relative absolute differences from each field at each measurement point in case of this second configuration are shown in Table 10.

Field	Reference point 4			Reference point 6		
	Planned [cGy]	Measured [cGy]	Difference [%]	Planned [cGy]	Measured [cGy]	Difference [%]
1/1/1	61.6	66.25	1.55	10.6	9.62	0.33
1/1/2	65.6	62.27	1.11	107.0	104.39	0.87
1/1/3	69.2	72.63	1.14	9.3	9.69	0.13
1/2/1	40.8	41.30	0.17	6.4	6.48	0.03
1/2/2	31.5	32.18	0.23	30.2	28.35	0.62
1/2/3	19.3	20.48	0.39	8.6	8.57	0.01
2/1/1	0.2	0.58	0.13	0.2	0.56	0.12
2/1/2	0.4	1.29	0.30	0.5	1.45	0.32
2/1/3	0.6	1.29	0.23	1.1	1.55	0.15
2/2/1	1.6	1.76	0.05	1.9	1.56	0.11
2/2/2	0.9	1.21	0.10	1.2	1.42	0.07
2/2/3	0.2	0.50	0.10	0.2	0.48	0.09
Sum	291.9	301.74	3.28	177.2	174.12	1.03

Table 10: Calculated and measured doses inside the right lung (reference point 6) and near the left lung (reference point 4). The relative absolute difference between the planned and the measured doses was normed with the fraction dose (300 cGy).

In the third configuration, the abdominal region of the plan was positioned centrally within the phantom to investigate the dose of the PTV at a sufficiently homogeneous region. The dose distribution calculated by the treatment planning system is shown in Figure 15.

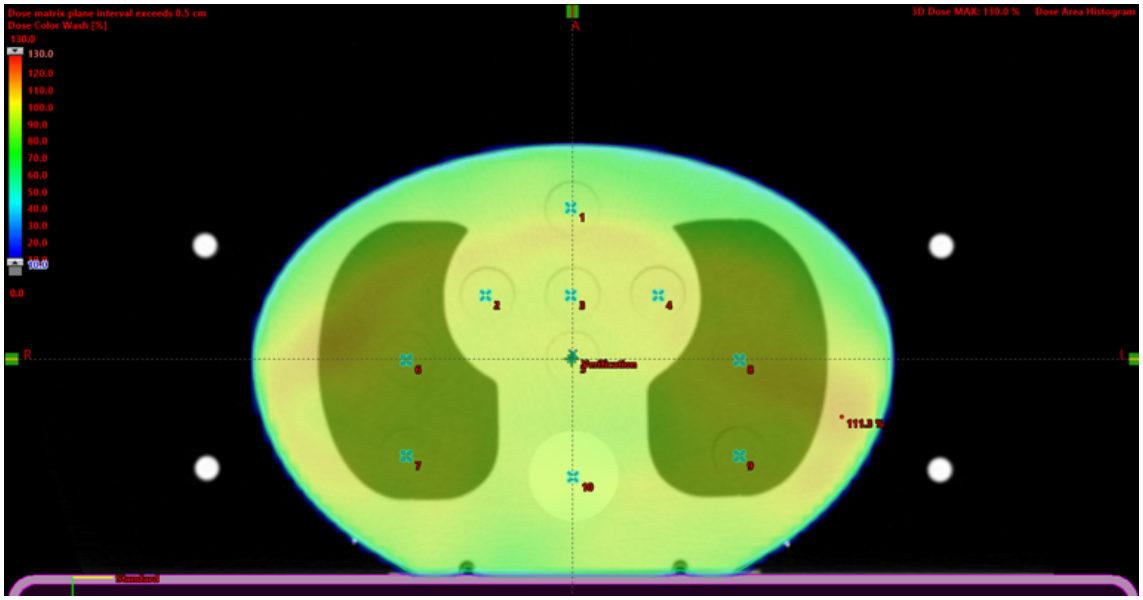

Figure 15: Third configuration for the absolute dose test: the abdomen's dose distribution is positioned to the central part of the CIRS phantom to investigate the dose of the PTV (inserts 2, 3, 4 and 5)

To investigate the dose received by this area, the third and fifth inserts were used. The dose to these points was delivered only by the fields of the middle isocenter. The calculated and the measured doses with their relative absolute differences from each field at each measurement point in case of this third configuration are shown in Table 11.

Field	Reference point 3			Reference point 5		
	Planned [cGy]	Measured [cGy]	Difference [%]	Planned [cGy]	Measured [cGy]	Difference [%]
2/1/1	22.6	22.74	0.05	5.2	6.08	0.29
2/1/2	211.7	207.81	1.30	213.2	210.63	0.86
2/1/3	7.2	8.08	0.29	3.9	5.07	0.39
2/2/1	5.2	5.95	0.25	2.1	2.96	0.29
2/2/2	45.7	53.00	2.43	73.5	73.99	0.16
2/2/3	3.3	4.04	0.25	1.8	2.60	0.27
Sum	295.7	301.62	1.97	299.7	301.33	0.54

Table 11: Calculated and measured doses at a homogeneous area, the abdomen (reference points 3 and 5). The relative absolute difference between the planned and the measured doses was normed with the fraction dose (300 cGy).

5 Discussion

5.1 Patient Cohort, Immobilization and CT

The patient cohort represents a limitation of this work. Since the study was based on retrospective CT scans, the patients were not scanned in the intended VMAT-TBI treatment position and did not use the proposed immobilization devices. Therefore, the achieved dose distributions reflect the feasibility of the planning method rather than the full clinical workflow. Most scans (Patients #1–6) did not include the entire body, and patients with unfavorable arm positions had to be excluded. This selection may have reduced anatomical variability.

Immobilization is an aspect that could not be validated directly in this study. While most components of the proposed immobilization setup are based on established clinical practice at the institute, their combined application in VMAT-TBI has not yet been validated. Furthermore, the introduction of a rotatable tabletop is a new feature at our institute, and its potential benefits in reducing setup uncertainties must be confirmed through future investigations.

CT resolution plays an important role in VMAT-TBI planning, as it directly influences contouring accuracy, dose calculation, and optimization times. In this work, a slice thickness of 1 cm was selected based on a finer resolution, which showed no relevant differences in dose distribution or DVHs apart from minor statistical variations. This finding suggests that coarser CT resolution may be sufficient, while reducing optimization time by 44.44%. Some articles [56, 57, 58, 69] mention the duration of certain processes: optimization and dose calculation times range from 5 hours [69] to 25-30 hours [58].

This result is more permissive than most recommendations in the literature, where slice thicknesses of 3–5 mm are preferred to ensure accurate representation of anatomical details [57, 58, 65, 68], near some example of the usage of 10 mm slice thicknesses[56, 58]. It should be noted that in case of TBI, the target volume is very large and dose gradients are generally smoother, which may reduce sensitivity to CT resolution, and clinical feasibility requires sensible computational times, which are not always achievable with finer resolutions.

5.2 Target Volume and Organs-At-Risk Determination

In this work, the PTV was generated by contracting the body contour by a few millimeters (4 mm in case of young children, 5 mm in other cases), in agreement with common practice reported in the literature [56, 57, 65, 69]. This method is applied to decrease dosimetric uncertainty in the superficial build-up region and to provide enough backscatter media.

The lungs and kidneys were excluded from the PTV to protect them from unnecessary damage. Additional margins were applied to these organs to facilitate dose reduction during optimization, hence improving the quality of the optimization. This method is commonly applied in the literature [56, 57]. In case of this work, the margin of the kidneys was set to 2 mm, while the margin of the lungs was dependent on the patients' size. It was 5 mm for adults and teenagers. In the case of the pediatric patient (Patient #7), lung margins were reduced to 4 mm to maintain a comparable ratio between spared organ volume and total body volume.

Some limitations must be acknowledged regarding the contouring process. Even though the cropped structures provide an ideal dataset for optimization, the widely adapted protocols should be interpreted within context, taking into account some physiological aspects. Since the ribs contain red bone marrow, it is a high priority to irradiate them properly [63], but due to the cropping, ribs might get out of the PTV during breathing. There are several studies in which rib coverage is investigated(e.g. [87, 88]), and this aspect should be taken into consideration in case of this method as well. The contouring method for this specific technique can be considered clinically acceptable if the appropriate rib coverage is ensured by measurements with phantoms simulating breathing motion.

5.3 Planning

Just like in many other works from the literature [56, 57, 58, 59, 69, 72], multiple isocenters with dual-arcs were used in this research. In some papers, VMAT arcs were distributed along the whole body [58, 65], while in case of this work, the lower extremities (whole legs or the upper thighs) were treated with AP/PA fields to reduce computational needs in case of patients whose height exceeded 115 cm, especially since there are no OARs at these areas. Some publication also follows this method [56], while other publications [57, 59, 69, 72] did not pay attention to this detail, since similarly to this work, they worked with retrospective CT scans obtained from head to upper thighs. In case of children whose height did not exceed 115 cm (Patient #7), VMAT arcs were placed along the whole body, since this process did not require more isocenters than the plans of taller patients with AP/PA fields. As a result, the plan of Patient #7 could be optimized in one stage, instead of optimizing AP/PA fields, then optimizing VMAT arcs, using the previous optimization as a base dose plan, like in case of patients above 115 cm of body height.

Even though the literature has examples of automated treatment planning [56], field placement happened manually in this work. Even though the field arrangements from the literature tried out here did not give sufficient dose distributions, there are aspects in which the details are similar. The VMAT fields were 18 cm x 40 cm and

20 cm x 40 cm, similarly to Symons *et al.*'s and Springer *et al.*'s work [57, 58]. On the other hand, even though the idea of Springer *et al.* to use more isocenters in the lateral direction [58] is remarkable, the reproduction of this arrangement did not give better results than simpler field arrangements. Given that 2-4 cm of overlap between fields is commonly used in the literature [57, 58, 59], the overlaps presented in Figures 6, 7 and 8 appear to be excessive.

In the literature, collimator rotations are generally 0°, 90° and 30° (e.g. [57, 58]), in contrast with the 10° and 350° of rotation in this work. Furthermore, in contrast with the 6 MV energy used by Springer *et al.* [58], 6FFF and 10X energies were used during this research, providing more degrees of freedom for the optimization software to reach deeper tissues.

Relatively fine dose-calculation grid sizes are typically recommended in the literature, with 5 mm being widely accepted as a practical compromise between spatial resolution and computational efficiency [57, 68, 70, 73, 74]. Although Acuros has been reported to provide improved accuracy in bone and lung tissue compared to the AAA algorithm [68], its use is associated with significantly increased computation times. In the present work, AAA was therefore selected to ensure clinically feasible planning times given the available computational resources. This choice represents a trade-off between calculation accuracy and workflow efficiency, which is a common consideration in clinical practice. The use of parallelized control-point-related calculation tasks and predefined processor and memory utilization limits influenced the achievable calculation times as well. Therefore, the runtime advantage of AAA observed in this work is specific to the available computational environment and may not be directly transferable to treatment planning systems with different hardware or service configurations.

To partially compensate for potential uncertainties related to dose calculation and delivery, additional planning constraints were introduced. The aperture shape control parameter was set to "low", limiting the formation of excessively small MLC apertures to enhance the robustness of plan delivery by reducing the sensitivity to mechanical uncertainties. The uniform application of predefined optimization objectives (Table 2) ensured consistency across all treatment plans, enabling a more reliable comparison of dosimetric outcomes between patients. The combined impact of algorithm selection, grid size, and modulation constraints should be considered when interpreting the results, as these factors may influence both dose homogeneity and the accuracy of dose estimation.

The observed effect of the autofeathering feature was unexpected, as its intended purpose is to smooth dose transitions between adjacent fields, thereby improving homogeneity. In contrast, the results of this study suggest that visually smoother dose distributions were achieved when autofeathering was turned off. This finding

is further supported by the dose profile analysis, which did not demonstrate the expected reduction in gradient steepness when autofeathering was applied. The profiles remained comparable, indicating that the feature did not produce the expected effect in the junction regions. One possible explanation for this is that such tools are typically optimized for conventional radiotherapy scenarios involving localized target volumes, where junction management occurs over relatively small scales. In the context of TBI, the larger treatment volume and extended field arrangements may limit the effectiveness of these built-in smoothing techniques. Consequently, the algorithm may not scale appropriately to the geometric challenges of VMAT-TBI. The absence of similar observations in the literature suggests that the behavior of autofeathering in TBI settings has not been systematically investigated.

This highlights an important practical aspect: not all planning system features are necessarily optimized for non-standard treatment techniques such as TBI. Therefore, reliance on default or theoretically beneficial options without empirical validation may lead to suboptimal planning procedure (e.g. in terms of optimization time if the given feature requires more calculation capacity). The application of planning tools should always be judged within the given clinical context, ideally evaluating them empirically, rather than assuming their universal applicability.

The dosimetric results demonstrated dependence of plan quality on patient size. While target coverage metrics (see Table 3) for "small" patients met or exceeded institutional criteria ($V_{90} > 95\%$, $V_{95} > 90\%$ and $D_2 < 110\%$) in most cases, "big" patients showed a noticeable degradation in coverage. In this work, multiple definitions of the homogeneity index (see Table 4) was calculated to make comparison with the literature possible. The obtained values show a similar tendency to the coverage regarding patient size, while the OAR doses did not show such pattern.

As shown in Table 3, when comparing the coverage data obtained for "small" patients with the corresponding values reported in the literature [56, 57, 58, 65, 66, 75, 76, 77], it can be generally observed that treatment plans are typically normalized to a higher dose level than in the present work. This is reflected in the fact that coverage metrics (V_{90}, V_{95}, D_{98}, D_{95}, D_{50}) are generally lower than those commonly reported in the literature, which are often associated with higher maximum dose values (D_5, D_2). In contrast, these high-dose metrics are lower in the results presented here. In this study, institutional guidelines were primarily followed ($V_{90} > 95$, $V_{95} > 90$, $D_2 < 110$), which are satisfied by the plans of "small" patients in cases of Patient#1 and Patient#5. In case of Patient#4, D_2 is slightly above the desired threshold, but this 0.03% of elevation compared to the institutional criterion is acceptable and can be explained by statistical variations. In case of Patient#7, whose plan contained only VMAT arcs from head to toe, all results regarding coverage are in agreement with these criteria.

The same tendency can also be observed for the OAR doses listed in Table 5. The mean lung and kidney doses of the "small" patients, including Patient#7, are within the ranges reported in the literature [56, 57, 58, 59, 66, 75], but they are positioned toward the lower part of these intervals. This is consistent with the lower target-dose metrics discussed above and further supports the assumption that the plans in the present work were normalized to a lower dose level, than those commonly reported in the literature. Consequently, the reduced high-dose levels were accompanied not only by lower maximum target doses, but also by relatively low mean doses to the lungs and kidneys. The applied planning protocol prioritized agreement with institutional dose constraints and OAR sparing, even if this resulted in slightly lower target coverage compared with some published data.

Homogeneity indices were generally in agreement with literature values [59, 66, 75, 76] for the "small" patients, including Patient#7, as shown in Table 4. Patient#4 exhibits a borderline deviation in one of the indices (HI_1), but the difference is minor and does not affect the overall consistency with published results, especially since the generally recommended metric by the ICRU83 is HI_2 [79]. This result indicates that the planning protocol presented in this work is theoretically able to provide sufficiently homogeneous dose distributions, which is a basic requirement of TBI.

In case of "big" patients, in-house criteria were satisfied only in case of Patient #6, while in other cases the coverage is so insufficient that it cannot be normed to a higher dose without making the maximum dose metrics unacceptably high. Since no normalization could achieve acceptable plans, Table 3 presents results achieved with normalizations similar to the "small" patients for the sake of comparison.

The OAR doses of the "big" patients follow the same interpretation. As shown in Table 5, the mean lung and kidney doses remain within the literature-reported ranges. The relatively low OAR doses in case of Patient #2 and #3 are probably a consequence of the insufficient coverage and the normalization to lower dose levels. If the plans were normalized upward in an attempt to improve target coverage, the doses to the lungs and kidneys would also be expected to increase. Therefore, in case of Patient#2 ans #3, acceptable OAR doses were achieved only in combination with inadequate target coverage, indicating that the main limitation was not organ sparing, but the inability to obtain a clinically acceptable balance between coverage and OAR protection. Given that the plan of Patient#6 showed sufficient coverage, the OAR doses in that case truly indicate the possibility of OAR protection.

Homogeneity indices were also strongly insufficient in case of Patient #2 and #3. On the other hand, Patient #6 can be considered borderline acceptable rather than clearly insufficient. Although HI_1 and HI_2 slightly exceed the literature-reported ranges, the deviations are modest, while HI_3 remains within the reported range.

Considering coverage metrics, OAR doses and homogeneity indices, the plans

were acceptable in case of "small" patients (Patients #1, #4, #5, #7) and of one "big" patient (Patient #6). Neither coverage nor homogeneity fulfilled the clinical expectations in case of Patient #2 and #3, who both belong to the "big" patient group. In case of Patient#3, VMAT arcs were used in the hip area instead of AP/PA fields, since the latter ones could not cover the patient due to obesity, while Patient#2 had a larger skeletal frame. Even though Patient#6 was considered a "big" patient, they were comparably smaller than the other two patients in the group - apparently, they were closer in length to the largest "small" patient (Patient #1, length of 76.8 cm) than to the other "big" patients (88.5 cm and 97 cm) with a length of 81 cm (see Table 1).

5.4 Quality Assurance

5.4.1 Patient Specific Quality Assurance

Like in the case of metrics obtained from the treatment planning system, the results revealed distinction between the performance of plans for "small" and "big" patients.

For "small" patients, including Patient#7, gamma passing rates were consistently high, overall exceeding the commonly accepted threshold of 95% for the 3%/3 mm criterion [57, 81] (see Table 6). This was observed for the overall evaluation, while within clinically relevant structures such as the PTV and lungs, some of the passing rates (Patients #4 and #5, respectively) were between 94% and 95%. Such small reductions may arise from dose calculation differences in regions with high dose gradients, where even slight discrepancies can lead to local gamma failures without indicating clinically relevant dose errors.

The lower PTV-specific gamma passing rate (82.06%) observed for Patient#7 may be explained by the patient geometry. The arms were positioned relatively far apart, resulting in a less compact and less ideal body contour for VMAT optimization and dose verification. This geometry may have increased local dose-calculation discrepancies in the upper extremity regions, as can be seen in Figure 16, thereby reducing the PTV gamma passing rate. Since the overall gamma passing rate and the OAR-specific passing rates remained high, this suggests that the discrepancy was localized rather than representative of a general failure of the plan.

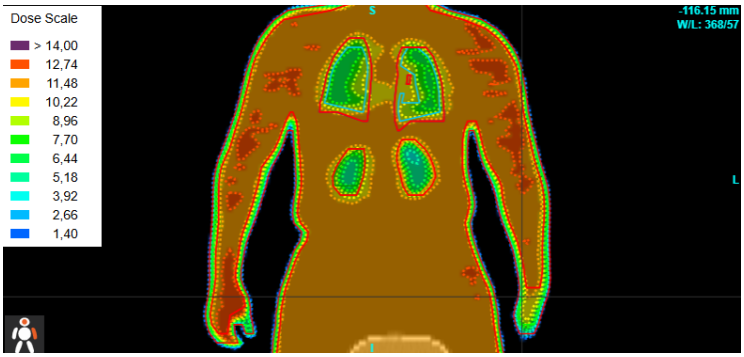

(a) Treatment planning system (Varian Eclipse)

(b) DoseCHECK

Figure 16: Dose distribution at the upper extremities of Patient #7

Relative differences in case of "small" patients remained within a few percent for both point (see Table 7) and mean (see Table 8) doses across all evaluated structures. On average, lung doses showed the biggest difference both in case of point (3.27% on average) and mean doses (2.74% for Patients #1, #4 and #5), which are clinically acceptable within our in-house protocols. In case of Patient #7, the difference of the mean PTV doses turned out to be quite elevated (6.7%), which might be explained by the same condition described in case of the gamma passing scores. It is worth denoting that the overall gamma passing rate for this patient was 99.04%, and the evaluation of this single metric would have masked the elevated mean PTV dose difference.

These results indicate good agreement between the treatment planning system and the independent dose calculation, suggesting that the plans are reliably deliverable in case of a real clinical situation, where immobilization provides a more ideal patient geometry for the planning procedure.

In contrast, the patient specific QA results for the "big" patients are less promising. While the QA results of Patient #2 were close to clinical acceptability, Patients#3 and #6 exhibited reduced gamma passing rates, especially in the PTV. The extremely low values observed for Patient#3 (33.15% overall passing rate, see Table 6) indicate a significant discrepancy between calculated and independently verified dose distributions, raising concerns about the reliability of dose delivery in

such cases. Patient#6's plan, although acceptable in terms of coverage and homogeneity, still demonstrates low QA performance, suggesting that acceptable plan quality does not guarantee deliverability in case of bigger patients. The reason behind the difference could be that DoseCHECK uses a different calculation algorithm (CCCS - collapsed cone convolution/superposition algorithm [89]).

Point and mean dose deviations (Tables 7 and 8, respectively) in these cases showed corresponding tendencies as the gamma passing rates. In case of Patient#3, differences up to 4.8% and 7.56% were observed for point and mean dose differences, respectively, while these values were up to 5.9% and 4.91% for Patient#6. The differences in case of Patient #2 were within the range of the values observed in case of "small" patients. Since Patient#3 and #6 were overweight, while Patient #2 is normal weight with a large skeletal frame, the independent calculation, and hence the simulated delivery, might fail due to the excess adipose tissue.

5.4.2 Absolute Dose Test

The absolute dose measurements demonstrated good agreement between the planned and measured doses. Across the three phantom configurations, the summed point-dose differences were between 0.52% and 3.28% when normalized to the fraction dose of 300 cGy. This result is in agreement with the similar measurement of Teruel *et al.*, where OSLDs were used with a CIRS phantom, and the dose deviations were ±4% [56]. Springer *et al.* performed MOSFET dosimetry, resulting in a difference between the planned and measured dose of 3.6% in the axilla and 4.3% in the wrist/hip-inguinal regions [58]. Tas *et al.* verified plans using DVH-based 3D patient QA systems (Dolphin and Compass), which demonstrated small differences between planned and delivered doses averaging 1.1%±0.7 for mean lung doses, 3.3%±1.3 for mean kidney doses, and 0.9%±0.4 for mean PTV doses. Even though these measurements in the literature are quite different in terms of devices, the comparison shows that the obtained differences shown in Tables 9, 10 and 11 are similar to these values.

The kidney configuration (see Table 9) showed particularly good agreement. The summed differences were 1.85% between the kidneys (reference point 3) and 0.52% in the left kidney (reference point 4).

For the lung configuration, the measured dose inside the lung-equivalent region agreed with the calculated dose within 1.03%. The largest summed deviation of the absolute dose test, 3.28%, was observed near the left lung (reference point 4) in the same configuration. There are two reasons behind this comparatively elevated difference. First of all, the fields of the middle isocenter did not explicitly cover the measurement points in this configuration. Unfortunately, in cases like this, the

treatment planning system underestimates the doses from such fields [90]. As it can be seen in Table 10, in case of reference point 4, the measured doses of the field of the middle isocenter are consistently higher than the planned doses for these fields. In fact, 2.37% of the total 3.28% difference came from these fields. The other reason behind the elevated dose difference is that the measurement point was at a high-gradient region. The ionization chamber has a finite sensitive volume, and the measured dose will be an average over this volume, while the calculation by the treatment planning system was performed for a single point. The ionization chamber itself was probably placed in a way that a slightly bigger volume was positioned at a higher-dose region, hence the measured average dose over this volume was higher than the point dose calculated by the treatment planning system. Even this highest discrepancy remained within a few percent, which is in agreement with the literature [56, 58, 59].

The third configuration investigated a relatively homogeneous abdominal region of the PTV. The summed differences were 1.97% and 0.54% at reference points 3 and 5, respectively. The good agreement in this homogeneous part of the phantom suggests that the treatment planning system and delivery system were able to reproduce the intended PTV dose accurately under conditions less affected by tissue heterogeneity and steep dose gradients.

6 Conclusion

The aim of this work was to develop a clinically feasible VMAT-based TBI planning workflow adapted to the technical conditions of our institute.

The results demonstrate that the proposed planning method is capable of producing acceptable treatment plans for some patients, with limitations regarding patient geometry.

The planning results indicate that acceptable target coverage and dose homogeneity can be achieved for smaller patients. All evaluated "small" patients fulfilled institutional criteria, and their dosimetric parameters were generally in agreement with values reported in the literature when differences in normalization strategies are taken into account. In addition, one patient categorized as "big" (Patient #6) also demonstrated acceptable coverage and homogeneity. However, this patient was closer in body length to the upper range of the "small" group than to the other "big" patients. The results imply the existence of an upper size threshold beyond which clinically acceptable plans cannot be achieved with the planning technique demonstrated here. Due to the limited cohort size, this threshold could not be determined in the present study and should be investigated in future work with a larger patient population.

Patient-specific QA results further emphasized the dependence of deliverability on patient characteristics. While the plans for smaller patients all showed agreement between planned and independently calculated dose distributions, the results for "big" patients were more diverse. Plans in case of overweight patients (Patients #3 and #6) showed reduced gamma passing rates and increased dose deviations, while the patient with normal weight and a larger skeletal frame (Patient #2) had QA results much closer to clinical acceptability. This observation suggests that excess adipose tissue, rather than overall body size, may affect the reliability of the delivery. Additional studies are required to evaluate this effect and to determine whether specific planning or calculation strategies could eliminate this limitation.

In case of Patient #7, a reduced gamma passing rate was observed in the PTV despite high overall and OAR-specific agreement. This discrepancy is related to the non-ideal arm positioning. This result emphasizes the importance of patient positioning and immobilization.

The absolute dose test confirmed that the planning protocol described in this work can be delivered with good dosimetric accuracy in target-like, kidney-related, and lung-related regions. The main limitation of the test was the lack of one-to-one anatomical correspondence between Patient #7 and the CIRS thorax phantom, which required separate configurations for different anatomical regions. Therefore, the measurement should be interpreted as a verification of representative dose-

delivery scenarios rather than a full anthropomorphic reproduction of the patient geometry. Despite this limitation, the agreement between calculated and measured doses supports the clinical feasibility of this workflow. In the literature, there are verification measurements using ArcCheck [57, 58] and Octavius phantom with an ionization chamber [69], providing the opportunity to perform gamma analysis, which is able to give information about the dose distribution as a whole, unlike point dose measurements, but performing only the latter also appears in articles [56, 58].

There are a few planning system features and clinical techniques reported in the literature that were not tried out in this work. For example, the use of spoilers or bolus materials, including gel boluses, has been suggested to improve dose build-up and surface dose coverage [58, 65]. Their potential benefits should be assessed in future studies.

Another aspect that has not been investigated in this work is the plans' robustness against setup uncertainties. Since small longitudinal misalignments can generate local over- or underdosage in junction regions, absolute dose testing frequently includes intentional couch shifts to simulate dose variations in case of positioning errors or patient movement [57, 59, 65].

Although image-guided verification represents an important component of VMAT-TBI, it was beyond the scope of the present work to investigate it in practice. In VMAT-TBI, cone-beam computed tomography (CBCT) is commonly acquired prior to irradiation at each isocenter (e.g. [66]) or at selected anatomical regions (e.g. head–neck, thorax, pelvis) [91] to match on-treatment images to the planning CT dataset. Registration is generally performed using bony anatomy, but Meyer *et al.*'s paper suggests registration based on gray value [92]. Surface-guided radiotherapy (SGRT) systems provide real-time monitoring of patient position using optical surface scanning. The acquired external surface is compared with a reference surface derived from the planning CT. SGRT is very advantageous in TBI, since long beam-on times could cause intrafraction motion which may compromise dose uniformity [75]. Furthermore, the absence of additional ionizing imaging dose represents a benefit, especially in pediatric patients. Although not strictly an imaging modality, in-vivo dosimetry is frequently used in TBI verification protocols. Semiconductor diodes, thermoluminescent dosimeters (TLDs), or MOSFET detectors [93] are positioned at representative anatomical sites (e.g. neck, oral cavity, hip, apical and basal lung) [94] to confirm the delivered dose during initial fractions. It is a natural direction for future work to incorporate image guided verification techniques to the technique described in this work.

In summary, the presented VMAT-TBI planning method is feasible for smaller patients, but limitations occurred for patients with larger body size, especially for those with increased adipose tissue. The QA results of Patient #7 drive attention to

the importance of patient positioning and immobilization in a way to ensure compact geometry. Future work should focus on investigating size-related feasibility limits, robustness against setup variations, and image guided verification techniques. The planning technique presented here should be modified to match the cases of bigger patients.

Acknowledgements

I would like to express my gratitude to my supervisor, Dr. Tamás Pócza, whose guidance and support have been invaluable throughout this work. I truly appreciated not only his professional advice, but also his friendly and approachable attitude, which made working with him a very positive and motivating experience.

I am also very grateful to Domonkos Szegedi from the hungarian National Institute of Oncology, who introduced me to the current institutional technique and helped me getting familiar with the treatment planning system.

I would also like to thank the institute for providing me with the opportunity to carry out this research and for offering the necessary environment and resources to complete my work. I am grateful to my internal supervisor, Dr. Csilla Pesznyák, for her role in coordinating the university-side supervision of this thesis and for providing me the connection to the institute.

Last but not least, I would like to thank my loved ones for their support and encouragement throughout my master's studies. I am especially grateful to my mother, Nóra Répás, my father, Tibor Kis, my sister, Klaudia Kis, my significant other, Dávid Attila Ködmön, and my best friend, Botond Zsigri.

References

[1] Lederman M. The early history of radiotherapy: 1895–1939. International Journal of Radiation Oncology*Biology*Physics. 1981 May;7(5):639–48. doi:10.1016/0360-3016(81)90379-5

[2] Holsti LR. Development of clinical radiotherapy since 1896. Acta Oncologica. 1995 Jan;34(8):995–1003. doi:10.3109/02841869509127225

[3] Huh HD, Kim S. History of radiation therapy technology. Progress in Medical Physics. 2020 Sept 30;31(3):124–34. doi:10.14316/pmp.2020.31.3.124

[4] Gianfaldoni S, Gianfaldoni R, Wollina U, Lotti J, Tchernev G, Lotti T. An overview on radiotherapy: From its history to its current applications in dermatology. Open Access Macedonian Journal of Medical Sciences. 2017 Jul 18;5(4):521–5. doi:10.3889/oamjms.2017.122

[5] Connell PP, Hellman S. Advances in radiotherapy and implications for the next century: A historical perspective. Cancer Research. 2009 Jan 15;69(2):383–92. doi:10.1158/0008-5472.can-07-6871

[6] Loginova AA, Nechesnyuk AA, Kobyzeva DA, Chernyaev AP, Varzar SM. Development of total body irradiation method. From history to the present. Pediatric Hematology/Oncology and Immunopathology. 2018 Sept 24;17(3):133–9. doi:10.24287/1726-1708-2018-17-3-133-139

[7] Thomas ED, Lochte HL, Lu WC, Ferrebee JW. Intravenous infusion of bone marrow in patients receiving radiation and chemotherapy. New England Journal of Medicine. 1957 Sept 12;257(11):491–6. doi:10.1056/nejm195709122571102

[8] Thomas E, Buckner C, Banaji M, Clift R, Fefer A, Flournoy N, *et al.* One hundred patients with acute leukemia treated by chemotherapy, total body irradiation, and allogeneic marrow transplantation. Blood. 1977 Apr 1;49(4):511–33. doi:10.1182/blood.v49.4.511.511

[9] Thomas ED, Buckner CD, Clift RA, Fefer A, Johnson FL, Neiman PE, *et al.* Marrow Transplantation for acute nonlymphoblastic leukemia in first remission. New England Journal of Medicine. 1979 Sept 13;301(11):597–9. doi:10.1056/nejm197909133011109

[10] Keane JT, Fontenla DP, Chui CS. Applications of IMAT to total body radiation (TBI). International Journal of Radiation Oncology*Biology*Physics. 2000 Jan;48(3):239. doi:10.1016/s0360-3016(00)80274-6

[11] Joiner M, Van Der Kogel A, editors. Basic clinical radiobiology. London: Edward Arnold; 2009.

[12] Robert Grimes D, Partridge M. A mechanistic investigation of the oxygen fixation hypothesis and oxygen enhancement ratio. Biomedical Physics & Engineering Express. 2015 Dec 4;1(4). doi: 10.1088/2057-1976/1/4/045209

[13] Khazaei Monfared Y, Heidari P, Klempner SJ, Mahmood U, Parikh AR, Hong TS, *et al.* DNA damage by radiopharmaceuticals and mechanisms of cellular repair. Pharmaceutics. 2023 Dec 12;15(12):2761. doi:10.3390/pharmaceutics15122761

[14] Mehta A, Haber JE. Sources of DNA double-strand breaks and models of recombinational DNA repair. Cold Spring Harbor Perspectives in Biology. 2014 Aug 7;6(9). doi:10.1101/cshperspect.a016428

[15] Lieber MR. Pathological and physiological double-strand breaks. The American Journal of Pathology. 1998 Nov;153(5):1323–32. doi:10.1016/s0002-9440(10)65716-1

[16] Sage E, Shikazono N. Radiation-induced clustered DNA lesions: Repair and mutagenesis. Free Radical Biology and Medicine. 2017 Jun;107:125–35. doi:10.1016/j.freeradbiomed.2016.12.008

[17] Morgan MA, Lawrence TS. Molecular pathways: Overcoming radiation resistance by targeting DNA damage response pathways. Clinical Cancer Research. 2015 Jun 30;21(13):2898–904. doi:10.1158/1078-0432.ccr-13-3229

[18] Mladenova V, Mladenov E, Stuschke M, Iliakis G. DNA damage clustering after ionizing radiation and consequences in the processing of chromatin breaks. Molecules. 2022 Feb 24;27(5):1540. doi:10.3390/molecules27051540

[19] Wang C, Lees-Miller SP. Detection and repair of ionizing radiation-induced DNA double strand breaks: New developments in nonhomologous end joining. International Journal of Radiation Oncology*Biology*Physics. 2013 Jul;86(3):440–9. doi:10.1016/j.ijrobp.2013.01.011

[20] Mao Z, Bozzella M, Seluanov A, Gorbunova V. DNA repair by nonhomologous end joining and homologous recombination during cell cycle in human cells. Cell Cycle. 2008 Sept 15;7(18):2902–6. doi:10.4161/cc.7.18.6679

[21] Mjelle R, Hegre SA, Aas PA, Slupphaug G, Drabløs F, Sætrom P, *et al.* Cell cycle regulation of human DNA repair and chromatin remodeling genes. DNA Repair. 2015 Jun;30:53–67. doi:10.1016/j.dnarep.2015.03.007

[22] Heylmann D, Ponath V, Kindler T, Kaina B. Comparison of DNA repair and radiosensitivity of different blood cell populations. Scientific Reports. 2021 Jan 28;11(1). doi:10.1038/s41598-021-81058-1

[23] Kwok M, Agathanggelou A, Stankovic T. DNA damage response defects in hematologic malignancies: Mechanistic insights and therapeutic strategies. Blood. 2024 May 23;143(21):2123–44. doi:10.1182/blood.2023019963

[24] Heylmann D, Ponath V, Kindler T, Kaina B. Comparison of DNA repair and radiosensitivity of different blood cell populations. Scientific Reports. 2021 Jan 28;11(1). doi:10.1038/s41598-021-81058-1

[25] Nishibuchi I, Tashiro S. DNA double-strand break repair capacity and normal tissue toxicity induced by radiotherapy. Journal of Radiation Research. 2024 Dec;65(Supplement_1):i52–6. doi:10.1093/jrr/rrae081

[26] Li N, Chen H, Wang J. DNA damage and repair in the hematopoietic system. Acta Biochimica et Biophysica Sinica. 2022 Jan 1;54(6):847–57. doi:10.3724/abbs.2022053

[27] Sabloff M, Tisseverasinghe S, Babadagli ME, Samant R. Total body irradiation for hematopoietic stem cell transplantation: What can we agree on? Current Oncology. 2021 Feb 14;28(1):903–17. doi:10.3390/curroncol28010089

[28] Jiao Y, Cao F, Liu H. Radiation-induced cell death and its mechanisms. Health Physics. 2022 Sept 6;123(5):376–86. doi:10.1097/hp.0000000000001601

[29] Zhang Y, Chen X, Wang X, Chen J, Du C, Wang J, *et al.* Insights into ionizing radiation-induced bone marrow hematopoietic stem cell injury. Stem Cell Research & Therapy. 2024 Jul 23;15(1). doi:10.1186/s13287-024-03853-7

[30] Paganetti H. A review on lymphocyte radiosensitivity and its impact on radiotherapy. Frontiers in Oncology. 2023 Aug 3;13. doi:10.3389/fonc.2023.1201500

[31] Qian S, Wei Z, Yang W, Huang J, Yang Y, Wang J. The role of BCL-2 family proteins in regulating apoptosis and cancer therapy. Frontiers in Oncology. 2022 Oct 12;12. doi:10.3389/fonc.2022.985363

[32] Baatout S. Radiobiology textbook. Cham, Switzerland: Springer; 2023.

[33] Garibaldi C, Jereczek-Fossa BA, Marvaso G, Dicuonzo S, Rojas DP, Cattani F, *et al.* Recent advances in Radiation oncology. Ecancermedicalscience. 2017 Nov 30;11. doi:10.3332/ecancer.2017.785

[34] Emami B, Woloschak G, Small W. Beyond the linear quadratic model: intraoperative radiotherapy and normal tissue tolerance. Translational Cancer Research. 2015 Apr;4(2):140–7. doi: 10.3978/j.issn.2218-676X.2015

[35] Wheldon TE. The radiobiological basis of total body irradiation. The British Journal of Radiology. 1997 Dec 1;70(840):1204–7. doi:10.1259/bjr.70.840.9505837

[36] Wong JYC, Filippi AR, Dabaja BS, Yahalom J, Specht L. Total body irradiation: Guidelines from the International Lymphoma Radiation Oncology Group (ILROG). International Journal of Radiation Oncology*Biology*Physics. 2018 Jul;101(3):521–9. doi:10.1016/j.ijrobp.2018.04.071

[37] Quast U. Whole body radiotherapy: A total body irradiation-guideline. Journal of Medical Physics. 2006;31(1):5. doi:10.4103/0971-6203.25664

[38] Hoeben BA, Wong JY, Fog LS, Losert C, Filippi AR, Bentzen SM, *et al.* Total Body Irradiation in Haematopoietic Stem Cell Transplantation for Paediatric Acute Lymphoblastic leukaemia: Review of the literature and Future Directions. Frontiers in Pediatrics. 2021 Dec 3;9. doi:10.3389/fped.2021.774348

[39] Peters C, Dalle J-H, Locatelli F, Poetschger U, Sedlacek P, Buechner J, *et al.* Total body irradiation or chemotherapy conditioning in childhood ALL: A multinational, randomized, Noninferiority Phase III study. Journal of Clinical Oncology. 2021 Feb 1;39(4):295–307. doi:10.1200/jco.20.02529

[40] Paix A, Antoni D, Waissi W, Ledoux M-P, Bilger K, Fornecker L, *et al.* Total body irradiation in allogeneic bone marrow transplantation conditioning regimens: A Review. Critical Reviews in Oncology/Hematology. 2018 Mar;123:138–48. doi:10.1016/j.critrevonc.2018.01.011

[41] Jung J, Lee H, Suh Y-G, Eom H-S, Lee E. Current use of Total body irradiation in haploidentical allogeneic hematopoietic stem cell transplantation. Journal of Korean Medical Science. 2021 Mar 1;36(8). doi:10.3346/jkms.2021.36.e55

[42] Inagaki J, Nagatoshi Y, Kawano Y, Saito Y, Takahashi D, Nagayama J, *et al.* Bone marrow transplantation in children with severe aplastic anemia using a conditioning regimen containing 3 Gy of total body irradiation, cyclophosphamide with or without antithymocyte globulin. Pediatric Transplantation. 2006 Nov 27;11(2):180–6. doi:10.1111/j.1399-3046.2006.00640.x

[43] Lv M, He Y, Yang D, Ma Q, Pang A, Zhai W, *et al.* Total body irradiation versus chemotherapy myeloablative conditioning in B-cell acute lymphoblastic

leukaemia patients with first complete remission. Scientific Reports. 2025 Mar 24;15(1). doi:10.1038/s41598-025-94556-3

[44] Espinoza-Gutarra M, Mohty R, Jamy O. Radiation-free conditioning in Acute lymphoblastic leukemia: Is it time? Chinese Clinical Oncology. 2024 Apr;13(2):29–29. doi:10.21037/cco-23-115

[45] IAEA. V-Chart of Nuclides [Internet]. Vienna: International Atomic Energy Agency; [cited 2025 Sep 30]. Available from: https://www-nds.iaea.org/relnsd/vcharthtml/VChartHTML.html#dcy1

[46] Ganz JC. The journey from Proton to Gamma Knife. Progress in Brain Research. 2014;215:67–75. doi:10.1016/b978-0-444-63520-4.00007-7

[47] Joslin CA, Smith CW. High and low dose rate afterloading techniques in radiotherapy [*Abridged*]. Proceedings of the Royal Society of Medicine. 1970 Oct;63(10):1029–34. doi:10.1177/003591577006301028

[48] Evans MDC, Larouche R, Olivares M, Léger P, Larkin J, Freeman CR, *et al.* Total body irradiation with a reconditioned Cobalt Teletherapy Unit. Journal of Applied Clinical Medical Physics. 2006 Feb 21;7(1):42–51. doi:10.1120/jacmp.v7i1.2175

[49] Kawa-Iwanicka A, Dybek M, Iwanicki T, Łobodziec W, Radkowski A. The technique of total body irradiation applied at the Leszczyński Memorial Hospital. Reports of Practical Oncology & Radiotherapy. 2002;7(2):53–60. doi:10.1016/s1507-1367(02)70979-6

[50] Wills C, Cherian S, Yousef J, Wang K, Mackley HB. Total body irradiation: A practical review. Applied Radiation Oncology. 2016 Jun 1;11–7. doi:10.37549/aro1097

[51] Hussein S, El-Khatib E. Total body irradiation with a sweeping 60Cobalt beam. International Journal of Radiation Oncology*Biology*Physics. 1995 Sept;33(2):493–7. doi:10.1016/0360-3016(95)00164-t

[52] Khan FM. The Physics of Radiation Therapy. Philadelphia: Lippincott Williams et Wilkins; 2003.

[53] Kaliyaperumal V, Kataria T, Tamilselvan S, Gupta D, Abraham S, Narang K, *et al.* Optimal combination of pitch, modulation factor and dosimetric considerations in treatment planning for total body irradiation using Helical Tomotherapy. Asian Pacific Journal of Cancer Prevention. 2023 Apr 1;24(4):1239–48. doi:10.31557/apjcp.2023.24.4.1239

[54] Hong C-S, Kim M-J, Kim J, Chang KH, Park K, Kim DW, *et al.* Feasibility of hybrid Tomohelical- and Tomodirect-based volumetric gradient matching technique for total body irradiation. Radiation Oncology. 2019 Dec;14(1). doi:10.1186/s13014-019-1435-5

[55] Losert C, Shpani R, Kießling R, Freislederer P, Li M, Walter F, *et al.* Novel rotatable tabletop for total-body irradiation using a LINAC-based VMAT technique. Radiation Oncology. 2019 Dec;14(1). doi:10.1186/s13014-019-1445-3

[56] Teruel JR, Taneja S, Galavis PE, Osterman KS, McCarthy A, Malin M, *et al.* Automatic treatment planning for VMAT-based total body irradiation using Eclipse scripting. Journal of Applied Clinical Medical Physics. 2021 Feb 10;22(3):119–30. doi:10.1002/acm2.13189

[57] Symons K, Morrison C, Parry J, Woodings S, Zissiadis Y. Volumetric modulated arc therapy for total body irradiation: A feasibility study using Pinnacle^3 treatment planning system and Elekta Agility^{TM} linac. Journal of Applied Clinical Medical Physics. 2018 Jan 24;19(2):103–10. doi:10.1002/acm2.12257

[58] Springer A, Hammer J, Winkler E, Track C, Huppert R, Böhm A, *et al.* Total body irradiation with volumetric modulated arc therapy: Dosimetric Data and first clinical experience. Radiation Oncology. 2016 Mar 22;11(1). doi:10.1186/s13014-016-0625-7

[59] Tas B, Durmus IF, Okumus A, Uzel OE, Gokce M, Goksoy HS, *et al.* Total-body irradiation using LINAC-based volumetric modulated arc therapy: Its clinical accuracy, feasibility and reliability. Radiotherapy and Oncology. 2018 Aug 29;129(3):527–33. doi:10.1016/j.radonc.2018.08.005

[60] Yu A, Fahimian B, Million L, Hsu A. A robust and affordable table indexing approach for multi-isocenter dosimetrically matched fields. Cureus. 2017 May 23; doi:10.7759/cureus.1270

[61] Leech M, Coffey M, Mast M, Moura F, Osztavics A, Pasini D, *et al.* ESTRO ACROP guidelines for positioning, immobilisation and position verification of head and neck patients for radiation therapists. Technical Innovations & Patient Support in Radiation Oncology. 2017 Mar;1:1–7. doi:10.1016/j.tipsro.2016.12.001

[62] Sharmin MN, Ray DrD, Kaes DrM. Child friendly mandatory immobilization devices for radiotherapy: Balancing comfort and clinical necessity from a medical physicist's perspective for Bangladesh. Journal of Cancer Prevention & Current Research. 2024;15(5):97–101. doi:10.15406/jcpcr.2024.15.00559

[63] Lambri N, Dei D, Hernandez V, Castiglioni I, Clerici E, Crespi L, *et al.* Automatic planning of the lower extremities for total marrow irradiation using volumetric modulated arc therapy. Strahlentherapie und Onkologie. 2022 Nov 3;199(4):412–9. doi:10.1007/s00066-022-02014-0

[64] Gruen A, Ebell W, Wlodarczyk W, Neumann O, Kuehl JS, Stromberger C, *et al.* Total body irradiation (TBI) using helical tomotherapy in children and young adults undergoing stem cell transplantation. Radiation Oncology. 2013 Apr 15;8(1). doi:10.1186/1748-717x-8-92

[65] Pierce G, Balogh A, Frederick R, Gordon D, Yarschenko A, Hudson A. Extended SSD VMAT treatment for total body irradiation. Journal of Applied Clinical Medical Physics. 2018 Dec 27;20(1):200–11. doi:10.1002/acm2.12519

[66] Köksal M, Özkan O, Holderried T, Heine A, Brossart P, Gawish A, *et al.* Optimized conformal Total Bdy Irradiation with VMAT using a linear-accelerator-based radiosurgery treatment system in comparison to the Golden Standard Helical Tomotherapy. Cancers. 2023 Aug 23;15(17):4220. doi:10.3390/cancers15174220

[67] Oswald L, Al-Kadhimi S, Thorp N. Anaesthesia for paediatric radiotherapy: A narrative review. Anaesthesia. 2025 Jan 8;80(S2):44–53. doi:10.1111/anae.16499

[68] Seravalli E, Bosman ME, Han C, Losert C, Pazos M, Engström PE, *et al.* Technical recommendations for implementation of Volumetric Modulated Arc Therapy and Helical Tomotherapy Total Body Irradiation. Radiotherapy and Oncology. 2024 Aug;197:110366. doi:10.1016/j.radonc.2024.110366

[69] Chakraborty S, Cheruliyil S, Bharathan R, Muttath G. Total Body Irradiation using VMAT (RapidArc): A Planning Study of a novel treatment delivery method. International Journal of Cancer Therapy and Oncology. 2015 Feb 26;3(2). doi:10.14319/ijcto.0302.8

[70] Guo B, Sheen C, Murphy E, Magnelli A, Lu L, Cho Y, *et al.* Image-guided volumetric-modulated arc therapy of total body irradiation: An efficient workflow from simulation to delivery. Journal of Applied Clinical Medical Physics. 2021 Sept 4;22(10):169–77. doi:10.1002/acm2.13412

[71] Chen H, Doyle L, Kim JO, Reeves J, Bundalevski I, Koecher A, Massello S, Strasser J. Automatic planning script for volumetric-modulated arc therapy total body irradiation (VMAT-TBI) [poster]. AAPM 66th Annual Meeting & Exhibition; 2024 Jul 21–25; Los Angeles, CA

[72] Tas B, Durmus IF, Okumus A, Uzel OE. Dosimetric evaluation of total body irradiation (TBI) treatment by volumetric modulated arc therapy (VMAT) on the coach. Journal of Biochemistry and Biophysics. 2017 Nov 28;1(1). doi:10.15744/2576-7623.1.103

[73] Salz H, Bohrisch B, Howitz S, Banz N, Weibert K, Wiezorek T, *et al.* Intensity-modulated total body irradiation (TBI) with TomoDirect^{TM}. Radiation Oncology. 2015 Mar 6;10(1). doi:10.1186/s13014-015-0362-3

[74] Cheung MM, Cheng AC, Lee L. Feasibility of segmental total body irradiation (SegTBI) using a 1.5T MR-linac. Journal of Applied Clinical Medical Physics. 2025 Jul;26(7). doi:10.1002/acm2.70192

[75] Sandt M, Marcet S, Guesnel N, Claude L, Martel I, Biston M-C. Implementation of LINAC-based VMAT total body irradiation technique on Elekta platform using surface-guided radiation therapy. Physica Medica. 2025 Mar;131:104940. doi:10.1016/j.ejmp.2025.104940

[76] Venugopal S, Khanna D, Mohandass P, Arya R. Dosimetric evaluation and feasibility of total body irradiation with multiple isocenter VMAT technique on the halcyon E ring gantry linear accelerator using photon optimizer algorithm. Journal of Cancer Research and Therapeutics. 2025 Apr;21(3):634–43. doi:10.4103/jcrt.jcrt_2411_24

[77] Köksal M, Kersting L, Schoroth F, Garbe S, Koch D, Scafa D, *et al.* Total marrow irradiation versus total body irradiation using intensity-modulated helical tomotherapy. Journal of Cancer Research and Clinical Oncology. 2023 Jan 6;149(9):5965–73. doi:10.1007/s00432-022-04565-2

[78] Kataria T, Sharma K, Subramani V, Karrthick K, Bisht S. Homogeneity index: An objective tool for assessment of conformal radiation treatments. Journal of Medical Physics. 2012;37(4):207. doi:10.4103/0971-6203.103606

[79] The International Commission on Radiation Units and measurements. Journal of the ICRU. 2010 Apr;10(1). doi:10.1093/jicru/ndq001

[80] Nirhali A, Naik V, Pagare R, Hunugundmath S, Deputy M, Gadhave S. No More Feet-first Supine: A Simplified Total Body Irradiation Planning and Delivery Using Single Head-first Supine CT Simulation and SGRT for Intra-fraction Motion Monitoring on Radixact Tomotherapy. International Journal of Clinical Oncology and Cancer Research. 2025 Jul 4;10(3):110–20. doi:10.11648/j.ijcocr.20251003.11

[81] Morrison CT, Symons KL, Woodings SJ, House MJ. Verification of junction dose between VMAT arcs of total body irradiation using a Sun Nuclear ArcCheck phantom. Journal of Applied Clinical Medical Physics. 2017 Oct 29;18(6):177–82. doi:10.1002/acm2.12208

[82] Low DA, Harms WB, Mutic S, Purdy JA. A technique for the quantitative evaluation of dose distributions. Medical Physics. 1998 May;25(5):656–61. doi:10.1118/1.598248

[83] Nelms BE, Simon JA. A survey on planar IMRT QA analysis. Journal of Applied Clinical Medical Physics. 2007 Jun;8(3):76–90. doi:10.1120/jacmp.v8i3.2448

[84] Zhen H, Nelms BE, Tomé WA. Moving from gamma passing rates to patient DVH-based QA Metrics in pretreatment dose QA. Medical Physics. 2011 Sept 19;38(10):5477–89. doi:10.1118/1.3633904

[85] Commissioning of radiotherapy treatment planning systems: Testing for typical external beam treatment techniques. Vienna: IAEA; 2011.

[86] Detectors for ionizing radiation [Internet]. [cited 2026 May 9]. Available from: https://www.ptwdosimetry.com/fileadmin/user_upload/Online_Catalog/DETECTORS_Cat_en_16522900_19/index.html?startpage=26

[87] Köksal M, Baumert J, Schoroth F, Scafa D, Koch D, Leitzen C, *et al.* Lung sparing and ribcage coverage in total body irradiation delivered by Helical Tomotherapy. European Journal of Medical Research. 2022 Dec 10;27(1). doi:10.1186/s40001-022-00918-2

[88] Loginova AA, Tovmasian DA, Lisovskaya AO, Kobyzeva DA, Maschan MA, Chernyaev AP, et al. Optimized conformal total body irradiation methods with Helical TomoTherapy and Elekta VMAT: Implementation, imaging, planning and dose delivery for pediatric patients. Frontiers in Oncology. 2022 Mar 10;12. doi:10.3389/fonc.2022.785917

[89] Dosecheck™ & Perfraction ™ on the accuracy of the SNC dose calculator algorithm [Internet]. Sun Nuclear Corporation; [cited 2026 May 28]. Available from: https://www.sunnuclear.com/uploads/documents/whitepapers/DC_PF_Accuracy-of-the-SNC-Dose-Calculator_091216.pdf

[90] Howell RM, Scarboro SB, Kry SF, Yaldo DZ. Accuracy of out-of-field dose calculations by a commercial treatment planning system. Physics in Medicine and Biology. 2010 Nov 12;55(23):6999–7008. doi:10.1088/0031-9155/55/23/s03

[91] Ouyang L, Folkerts M, Zhang Y, Hrycushko B, Lamphier R, Lee P, *et al.* Volumetric modulated arc therapy based total body irradiation: Workflow and clinical experience with an indexed rotational immobilization system. Physics and Imaging in Radiation Oncology. 2017 Oct;4:22–5. doi:10.1016/j.phro.2017.11.002

[92] Meyer J, Wilbert J, Baier K, Guckenberger M, Richter A, Sauer O, *et al.* Positioning accuracy of cone-beam computed tomography in combination with a hexapod robot treatment table. International Journal of Radiation Oncology*Biology*Physics. 2007 Mar;67(4):1220–8. doi:10.1016/j.ijrobp.2006.11.010

[93] Bloemen-van Gurp EJ, Mijnheer BJ, Verschueren TAM, Lambin P. Total body irradiation, toward optimal individual delivery: Dose evaluation with metal oxide field effect transistors, thermoluminescence detectors, and a treatment planning system. International Journal of Radiation Oncology*Biology*Physics. 2007 Nov;69(4):1297–304. doi:10.1016/j.ijrobp.2007.07.2334

[94] Carminati S, Trivellato S, Ingraito C, Montanari G, Morzenti S, Paruccini N, *et al.* In vivo dosimetry of total body irradiation patients: A 10 year retrospective analysis. Physica Medica. 2024 Oct;126:104831. sdoi:10.1016/j.ejmp.2024.104831